

Enhancing Hemodynamic Parameter Estimations: Nonlinear Blood Behavior in 4D Flow MRI

Hernán Mella^{a,*}, Felipe Galarce^{b,*}, Tetsuro Sekine^c, Julio Sotelo^d, Ernesto Castillo^e

^aSchool of Electrical Engineering, Pontificia Universidad Católica de Valparaíso, Av. Brasil 2147, Valparaíso, 2340000, Chile

^bSchool of Civil Engineering, Pontificia Universidad Católica de Valparaíso, Av. Brasil 2147, Valparaíso, 2340000, Chile

^cDepartment of Radiology, Nippon Medical School Musashi Kosugi Hospital, Kanagawa, 2118533, Japan

^dDepartamento de Informática, Universidad Técnica Federico Santa María, Santiago, 8940000, Chile

^eDepartment of Mechanical Engineering, Universidad de Santiago de Chile, Santiago, 9160000, Chile

Abstract

Hemodynamic parameters are often estimated assuming a constant Newtonian viscosity, even though blood exhibits shear-thinning behavior. This article investigates the influence of blood rheology and hematocrit (Hct) percentage on the estimation of Wall Shear Stress (WSS), rate of viscous Energy Loss (\dot{E}_L) at different points in the cardiac cycle, and the Oscillatory Shear Index (OSI). We focus on a hematocrit-dependent power-law non-Newtonian model, considering a wide range of Hct values at physiological temperature, with rheological parameters obtained from previously reported experimental data. In all cases, we systematically compared WSS, \dot{E}_L , and OSI using both Newtonian and power-law models, underscoring the crucial role of blood rheology in accurately assessing cardiovascular diseases. Our results show that, in in-silico experiments, differences in WSS and \dot{E}_L across a wide range of Hct values can reach as high as 190% and 113% at systole, and as low as -72% and -74% at diastole, respectively. In in-vivo data, differences in WSS and \dot{E}_L can reach up to -45% and -60% at systole, and range from -69% to 73% at diastole. This study enhances our understanding of the impact of blood rheology on hemodynamic parameter estimations using both in-silico and in-vivo aortic 4D Flow MRI data.

Keywords: 4D Flow MRI, Blood Rheology, Cardiovascular MRI, Hemodynamics, Finite Elements

1. Introduction

Hemodynamic parameters estimated from 4D Flow Magnetic Resonance (MR) images such as Wall Shear Stresses (WSS), Oscillatory Shear Indexes (OSI), and viscous Energy Loss (E_L) have been successfully used for the assessment of several cardiovascular diseases in large vessels, including Bicuspid Aortic Valve [1], aortic coarctations [2], stenosis [3], among others [4]. These parameters need as input a blood viscosity μ , which in most of the cases is assumed constant and within the range of 0.03 to 0.045 poise [5, 6, 7, 8, 9, 10]. This assumption has been accepted in the cardiovascular MRI community for the past decades, serving as the gold standard for the estimation of viscosity-dependent hemodynamic parameters from 4D Flow MR images. However, the blood viscosity has an intrinsic shear-thinning nonlinear behavior (i.e., viscosity decreases as the shear rates increases) that, to the author's knowledge, has not been systematically considered in estimating these parameters.

Blood is a non-homogeneous and non-linear fluid comprising red blood cells, white blood cells, and platelets suspended in plasma. The behavior of blood can be modeled using continuum mechanics and experimental data, leading to non-Newtonian constitutive models. Generally, blood exhibits shear-thinning behavior, primarily dependent on the hematocrit (Hct) percentage. This shear-thinning behavior can be effectively described using models such as the power-law [11, 12], Carreau-like [13, 14, 15], Cross [16, 12], and Casson models [17]. Considering that the power-law has been successfully fitted to a wide range of Hct percentages under physiological temperatures [18, 19, 20], we have adopted this model as a suitable candidate for explaining blood's fluid behavior.

* Authors contributed equally

Increased Hct can result from dehydration and polycythemia, while decreased values can be caused by anemia, overhydration, kidney failure, pregnancy, or chronic inflammatory conditions [21, 18, 19, 20, 22]. Although Hct can range from 10% to 70% in individuals with these conditions, the normal range is $47 \pm 7\%$ for men and $42 \pm 6\%$ for women [23]. Besides, shear rate depends on spatial and temporal blood flow characteristics, opening up the question of whether Newtonian modeling, accepted by the MRI community, truly represents a whole cardiac cycle. In this regard, including a non-Newtonian rheological behavior could generate potential differences in hemodynamic parameters across patients, especially in non-physiological blood conditions.

The influence of blood rheology has been studied in various hemodynamic contexts using 4D Flow MRI. For example, a shear-thinning viscosity model dependent on Hct was employed to estimate hemodynamic parameters from in-vivo 4D Flow data in the circle of Willis in children and adults with sickle cell disease [24], as well as for flow and hemodynamic analysis of the left ventricle [25]. In the latter study, two different rheology models were assessed and compared to state-of-the-art Newtonian viscosity estimations, revealing notable differences between models. In-silico studies, involving geometries resembling Fontan patients, as well as in-vitro 4D Flow MRI phantom experiments, were conducted in [26] to evaluate the impact of shear-dependent fluid viscosity on in-vitro Fontan circulation. A similar study assessed prosthetic heart valves using in-vitro experimental data obtained through Particle Imaging Velocimetry [27].

From a numerical standpoint, the hemodynamics community has largely advanced using the finite element method (FEM) [28, 29]. FEM has been extensively applied to analyze and solve the governing dynamics of the cardiovascular system, such as the Navier-Stokes equations and related models [30], and to compute full states and related parameters for inverse problems based on medical data [31, 32]. In [33], a numerical study investigated the influence of hematocrit levels in blood, considering both anemic and physiological patients in a simplified carotid artery model. The study found differences in vortex shedding frequency and flow bifurcation between the carotid outlet branches. In [34], a numerical analysis of aortic aneurysms evaluated non-Newtonian and Newtonian models through CFD simulations with two turbulence models, revealing small differences in flow dynamics and hemodynamic parameters across viscosity and turbulence models. Similarly, [35] assessed the arterial and venous systems through numerical experiments with different viscosity models, concluding that accounting for non-Newtonian behavior is crucial for cardiovascular flows exhibiting low shear rates and recirculation.

Despite the valuable insights provided by the aforementioned hemodynamics works where the shear-thinning rheological behavior has been incorporated in the blood flow modeling, it is essential to mention some limitations and open questions. The effect of rheological behavior in large vessels like the aorta has not been analyzed in detail [24, 25]. The impact of blood hematocrit has not been studied in wide ranges [26, 35, 34], or has not addressed their influence on specific hemodynamic parameters like WSS and OSI [27]. Additionally, none of these studies have evaluated whether, under common MR imaging conditions and issues such as partial volume effects, flow artifacts, and noise, the impact of the shear-thinning effect is still measurable.

In this work, we demonstrate that if blood exhibits shear-thinning behavior, this effect can be accurately measured from 4D Flow MRI data, even in the presence of imaging artifacts under common conditions. To support this claim, we conducted numerical and in-vivo experiments where hemodynamic parameters were estimated from 4D Flow data using both power-law and linear viscosity models for blood rheology. Comparisons were made for WSS, \dot{E}_L (rate of viscous E_L), and OSI estimations. Building upon these state-of-the-art models, this study integrates the 3D Navier-Stokes equations with 0D surrogate models for downstream flow and non-linear stress tensors to simulate shear-thinning blood behavior in experimental settings. Additionally, in-vivo experiments incorporate power-law viscosities adjusted to each patient's Hct, measured at physiological temperatures. This work contributes to a deeper understanding of blood rheology in MRI and CFD studies, laying the groundwork for more specific future investigations.

2. Theory and methods

2.1. Mathematical modeling

Let $\Omega \in \mathbb{R}^3$ be the three-dimensional computational domain, whose two-dimensional boundaries are decomposed in disjoint subsets such that $\partial\Omega = \Gamma_{\text{in}} \cup \bigcup_{k=1}^l \Gamma_{\text{out}}^k \cup \Gamma_{\text{wall}}$, referring Γ_{out} for the outlets, Γ_{in} for the inlet, and Γ_{wall} for the artery walls. The incompressible Navier-Stokes (NS) equations relates the velocity vector field (\mathbf{u}) and the pressure (p) field as follows:

$$\rho \frac{\partial \mathbf{u}}{\partial t} + \rho \mathbf{u} \cdot \nabla \mathbf{u} + \nabla p - \nabla \cdot \boldsymbol{\tau} = 0 \quad \text{in } \Omega, \quad (1a)$$

$$\nabla \cdot \mathbf{u} = 0 \quad \text{in } \Omega, \quad (1b)$$

$$\mathbf{u} = \mathbf{g}(x, t) \text{ on } \Gamma_{\text{in}}, \quad (1c)$$

$$\mathbf{u} = 0 \quad \text{on } \Gamma_{\text{wall}}, \quad (1d)$$

$$(\boldsymbol{\tau} - p\mathbf{I}) \cdot \mathbf{n} = -p_{\text{wk}}^k \text{ on } \Gamma_{\text{out}}^k, \quad (1e)$$

where $k = 1, \dots, l$ is the outlet counter, $\boldsymbol{\tau}$ denotes the shear stress tensor of the fluid, and ρ is the fluid density. We will discuss about modeling choices for $\boldsymbol{\tau}$ in the following section. Additionally, $\mathbf{g}(x, t)$ is an arbitrary spatially and temporarily dependent boundary condition used to define the pulsatile behavior of blood flow. To model the downstream fluid we couple the 3D-NS equations with the reduced 0D three-parameters Windkessel models [28] (see Figure 1), as it is typically done in the literature [36, 32, 37, 30]. This approach boils down to solving an ordinary differential equation (ODE) for each outlet domain, such that:

$$p_{\text{wk}}^k = R_p Q^k(\mathbf{u}) + p_d^k, \quad k = 1, \dots, l, \quad (2a)$$

$$C^k \frac{dp_d^k}{dt} + \frac{p_d^k}{R_d^k} = Q^k(\mathbf{u}), \quad k = 1, \dots, l. \quad (2b)$$

where $Q^k(\mathbf{u}) = \int_{\Gamma_{\text{out}}^k} \mathbf{u} \cdot ds$, and the parameters R_d^k, C^k, R_p^k , are the distal resistance, capacitance, and proximal resistance, respectively. The ODE should be closed with an adequate initial condition $p_{d,0}^k$. This configuration reproduces the downstream vascular tree and interacts with the 3D-NS model by setting an inwards force. It must be noted that we are using 0D parameters adjusted initially within a Newtonian context. It is a future endeavor of the researchers also to consider the blood rheology on the downstream fluid model.

2.2. On the choice for the shear stress blood behavior

In this work, we will estimate hemodynamic parameters using a Newtonian and a purely viscous shear-thinning blood behavior summarized below:

1. **Newtonian fluid behavior:** This is the gold standard in hemodynamics simulations and assumes that the shear stresses are proportional to the rate of change of the fluid's velocity vector. While this assumption is widely accepted for large blood vessels where the Reynolds number is also large, its applicability for systolic and diastolic conditions has not yet been thoroughly assessed using modern 4D-flow MRI. The model for a Newtonian fluid involves solving equations (1), where the shear stress is defined as $\boldsymbol{\tau} = 2\mu_N \dot{\boldsymbol{\epsilon}}$, with μ_N representing the constant viscosity of blood, and $\dot{\boldsymbol{\epsilon}}$ denoting the symmetric velocity gradient, which satisfies $2\dot{\boldsymbol{\epsilon}} = \nabla \mathbf{u} + \nabla^T \mathbf{u}$.
2. **Power-law fluid behavior:** Blood is a purely viscous shear-thinning fluid. It can be modeled using a generalized Newtonian law that accounts for strain-rate-dependent viscosity. The power-law model is a two parameters constitutive law that relates the shear stresses with the rate of change of the fluid's velocity vector as:

$$\boldsymbol{\tau} = \mu_{\text{PL}} \dot{\boldsymbol{\epsilon}}, \quad \text{with } \mu_{\text{PL}} = m \dot{\gamma}^{n-1} \quad (3)$$

where μ_{PL} denotes the apparent viscosity and $\dot{\gamma} = \sqrt{2\dot{\boldsymbol{\epsilon}} : \dot{\boldsymbol{\epsilon}}}$ the shear rate. The power-law index parameter n defines the rheological behavior of the fluid, with $n = 1$ corresponding to the Newtonian model. Shear-thinning fluids like blood are characterized by $n < 1$. The parameter m (with units $\text{Pa} \cdot \text{s}^n$), known as the consistency index, ensures dimensional consistency and allows the rheologist to adjust the apparent viscosity model to experimental discrete measurements. The values of the parameters m and n , fitted based on those proposed in [19, 20, 18], were derived from experimental studies and characterized at a physiological temperature of 37°C (see Table 1).

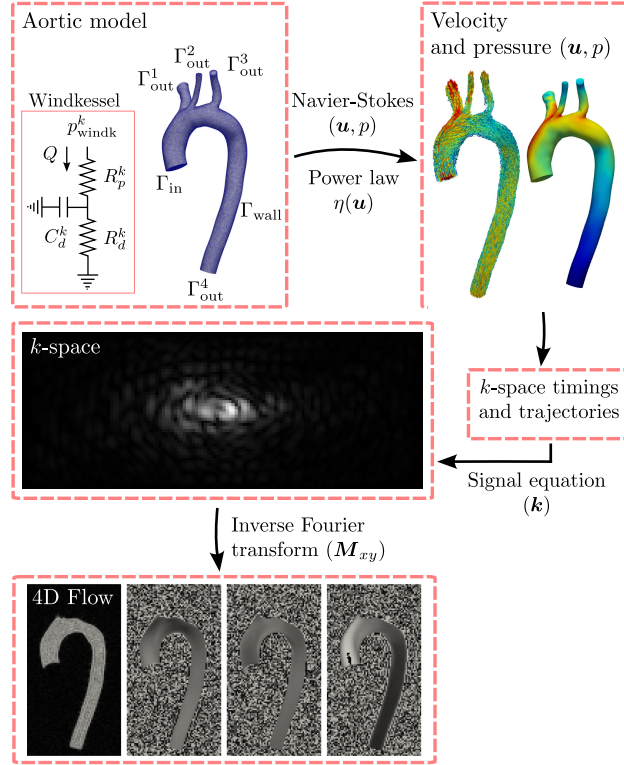


Figure 1: Simulation workflow for generating 4D Flow MR images. First, the aortic model serves as input to the MAD library, where the Navier-Stokes equations with nonlinear viscosity are solved. Subsequently, k -space locations and sequence timings are generated using parameters from Table 3, and the signal equation in (4) is evaluated. Trapezoidal MRI gradients are considered for the generation of sequence timings.

2.3. Signal model for 4D Flow images

The generation of 4D Flow MR images was based on the blood velocity $\mathbf{u} = (u_x, u_y, u_z)$ obtained from CFD simulations. The process involved evaluating the signal equation, which depends on the magnetization at thermal equilibrium $M_0(\mathbf{r})$, velocity encoding sensitivity (VENC), blood velocity u_a (with $a = x, y, z$), and the relaxation time of the blood $T_2^*(\mathbf{r})$. The signal equation is expressed as follows:

$$s^a(\mathbf{k}(t)) = \int_B M(\mathbf{r}, t) p(\mathbf{r}) e^{-i2\pi \mathbf{k}(t) \cdot \mathbf{r}(t)} d\mathbf{r}, \quad (4a)$$

$$M(\mathbf{r}, t) = M_0(\mathbf{r}) e^{-i\pi/\text{VENC} u_a(\mathbf{r})} e^{-t/T_2^*(\mathbf{r})}, \quad (4b)$$

In this formulation, $p(\mathbf{r})$ represents the slice profile, and $\mathbf{k}(t)$ denotes the Fourier space trajectory during signal acquisition, which varies based on the chosen imaging sequence. The integration domain B in the integral refers to the object being measured, in our case, the aorta. Careful consideration of scanner hardware limitations is required when determining the time t at which each $\mathbf{k}(t)$ location is measured. Factors such as the velocity, phase-encoding, and readout gradients, which depend on the maximum slew rate and amplitude of the gradient system, influence the echo time. Additionally, the readout gradient is affected by the sampling frequency of the ADC, which impacts not only the timing of each k -space measurement but also the occurrence of certain artifacts.

During signal measurement, the positions of spins change due to blood dynamics. This motion is accounted for using a first-order approximation of the spins' positions $\mathbf{r}(t)$ around t_k :

$$\mathbf{r}(t) = \mathbf{r}(t_k) + \mathbf{u}(t_k)(t - t_k) + \mathcal{O}(t^2), \quad (5)$$

where t_k represents the time where the image was taken.

No field inhomogeneities were considered during the evaluation of the signal equation, and the integral was calculated for each k -space location using the Finite Element Method (FEM). All the steps described here were implemented in a branch of the PyMRStrain library (github.com/hmella/pymrstrain/tree/4dflow), which has previously been used to generate synthetic strain phantoms [38, 39, 40]. The simulation workflow described in this section is illustrated in Figure 1.

2.4. Estimation of power-law parameters for custom Hct values and fitted-Newtonian viscosities

Viscosity measurements at 37° for different Hct values of 16%, 33%, 43%, 57%, and 70% across a shear rate range of 12 to 123 s^{-1} were obtained from [18]. Since the experimental data were not measured at the same shear rates, the parameters m and n in the power-law model described in (3) were fitted for the values provided in the article within a shear rate range of 10 to 130 s^{-1} . One-dimensional interpolations between these fits were then performed to generate synthetic experimental measurements at shear rates of 12.3, 24.4, 61.8, and 123.7 s^{-1} (mean shear rate across experimentally measured Hct values). These interpolated values were subsequently used to fit the power-law model over the same shear rate range described previously.

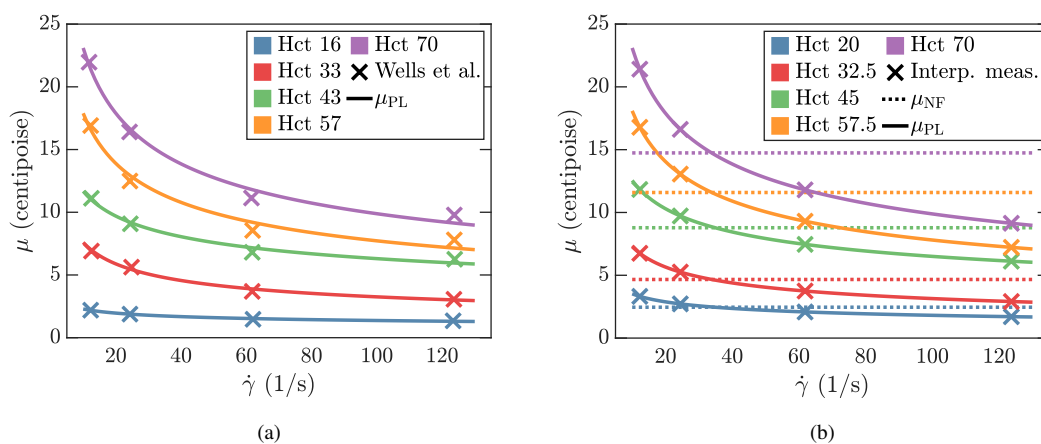


Figure 2: Viscosities obtained from Wells et al. [18]. (a) Experimental measurements and the adjusted power-law viscosities (μ_{PL}) derived from the data. (b) Synthetic measurements (obtained using one-dimensional linear interpolation), along with Newtonian fits (μ_{NF}) and power-law fits (μ_{PL}) for intermediate Hct levels not reported in [18]. Colors represent different Hct levels.

The power-law fit was performed using weighted least squares to account for unequal variances across shear rates and to avoid unwanted fitting biases. The Newtonian fit was carried out by estimating the mean value of the synthetic measurements, effectively solving a least squares problem for a constant model. The resulting viscosities are shown in Figure 2.

With this in mind, it is important to note that three different viscosities were considered in this investigation:

- μ_N : The Newtonian viscosity typically used in hemodynamic contexts (not fitted by Hct values).
- μ_{NF} : The Newtonian viscosity fitted to different Hct values.
- μ_{PL} : The non-linear viscosity estimated using the power-law model given in (3) and fitted to Hct values.

All of these viscosities are listed in Table 1 for Hct values of 20, 32.5, 45, 57.5, and 70, which were used in all experiments involving CFD simulations and synthetic images.

3. Experiments

3.1. Computational fluid dynamics for flow simulations

For all CFD experiments, the computational domain was set as a tetrahedral mesh of a patient-specific aorta model (see Figure 1), obtained from the Vascular Model Repository [2, 41, 42, 43]. The mesh consists of 127,131 vertices

Table 1: Viscosities used for CFD simulations and the estimation of hemodynamic parameters from synthetic and in-vivo 4D Flow images were obtained from [18] using the procedure described in Section 2.4. The parameters m and n were used to calculate μ_{PL} by evaluating Equation (3).

Hematocrit (%)	Newtonian μ_N (10^{-3} Pa·s)	Power-law ¹ m (10^{-2} Pa·s ^{n}), n	Newtonian fitted μ_{NF} (10^{-3} Pa·s)
<i>CFD experiments</i>			
20.0		0.6850, 0.7113	2.4571
32.5		1.7271, 0.6339	4.7578
45.0	3.0, 3.5, 4.0, 4.5	2.4208, 0.7146	8.7839
57.5		4.1933, 0.6349	11.5903
70.0		5.3985, 0.6313	14.7419
<i>In-vivo experiments</i>			
28.2		1.3604, 0.6506	-
35.2		1.8313, 0.6655	-
40.2	3.0, 3.5, 4.0, 4.5	2.0307, 0.7143	-
46.6		2.6352, 0.7015	-
50.1		3.1224, 0.6759	-

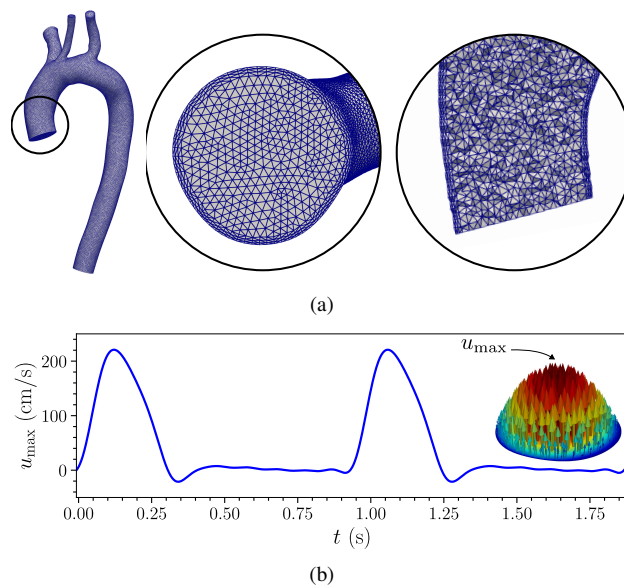


Figure 3: (a) Near-wall mesh refinement used in CFD simulations to capture velocity gradients accurately. (b) Inlet boundary condition $u_{max}(t)$ and parabolic flow profile applied as Dirichlet boundary conditions on Γ_{in} .

and 719,419 tetrahedrons, and it has been refined near the wall to account for boundary layer effects and to accurately represent spatial gradients (see Figure 3).

The governing equations of the flow given in (1) were solved using FEM with piece-wise linear Lagrange elements for \mathbf{u} and p . To overcome the well-known inf-sup constraints [44], a Brezzi-Pitkäranta stabilization term was added to the formulation [45], alongside a streamline upwind term to ensure stability for highly convective flows [46, 47]. Similar stabilization techniques in non-Newtonian fluids have been tested and analyzed in detail in [48, 49]. Additionally, the back-flow stabilization method proposed in [50, 51] was incorporated into all the simulations.

The inlet boundary condition, as defined in (1c), is represented by $g(x, t) = u_{max}(t)\mathcal{S}(x)$. Here, u_{max} is obtained from phase-contrast MRI measurements [2]. The function \mathcal{S} characterizes the spatial distribution of the Dirichlet condition, resembling a laminar parabolic fluid profile. Both u_{max} and \mathcal{S} are shown in Figure 3.

We employed a second-order finite difference formula for temporal discretization with a time step size of $\Delta t =$

9.37×10^{-4} s (equivalent to 1000 steps per cardiac cycle). The simulation covered two cardiac cycles, with only the last cycle considered in the analysis to avoid nonphysical solutions.

The non-linear terms in (1), i.e., the convection and the fluid constitutive, were linearized using a Picard fixed point approach, with an $H^1 \times L^2$ error tolerance of $\delta_p = 10^{-4}$. The coupling with the Windkessel model is done semi-implicitly, using a 4th-order Runge-Kutta scheme for the ODE.

We use the software MAD [52] to assemble the discrete equations and invert the linear systems. MAD is built upon the linear algebra library PETSc [53], and the computations are done with up to 72 CPU cores in parallel. A summary of the numerical simulation parameters is given in Table 2.

Table 2: Simulation parameters used for CFD simulations.

FEM parameter	Value
Time step (Δt)	9.37×10^{-4} sec
Nonlinear tolerance (δ_p)	10^{-4}
Backflow parameter (β) [50, 51]	0.2
Windkessel Parameter	$\Gamma_{\text{out}}^1, \Gamma_{\text{out}}^2, \Gamma_{\text{out}}^3, \Gamma_{\text{out}}^4$
Proximal resistance (R_p^k)	274, 1300, 791, 141
Distal resistance (R_d^k)	5675, 19663, 10048, 2066
Capacitance ($C^k \times 10^{-4}$)	5.08, 1.4416, 2.788, 13.6904
Distal pressure ($p_{d,0}^k$)	107325, 107325, 107325, 107325

3.2. Generation of synthetic 4D Flow images

To generate 4D Flow MR data, imaging parameters such as voxel size, number of cardiac phases, and VENC were selected according to the 2023 4D Flow MRI consensus (see Table 3) [54]. Hardware parameters, including maximum gradient amplitude, slew rate, and ADC frequency bandwidth, which dictated sequence timings and image quality, were taken from [55] and [56]. For each Hct, a gradient-echo image was simulated with a VENC slightly higher than the maximum velocity observed at peak systole to avoid wrapping artifacts.

To emulate realistic imaging conditions, Gaussian noise was introduced with a standard deviation set at 5.2% of the maximum amplitude of the complex signal’s magnitude, achieving an SNR of 13.5, which aligns with the average SNR reported for the ascending and descending aorta at 1.5T [57]. Noise was added to both the real and imaginary channels.

Finally, the MRI signals generated from CFD simulations, using the power-law model and constant viscosities adjusted for Hct, were reconstructed into 4D Flow images by performing the inverse Fourier transform of the signal, as defined in equation (4).

Table 3: Simulation parameters for the generation of synthetic 4D flow MR images. These parameters gave a echo-time of 1.66 ms.

Imaging parameter	Value
VENC (m/s)	2.5
Matrix size	$56 \times 30 \times 113$
Voxel size (mm^3)	$2 \times 2 \times 2$
Oversampling factor	2
Cardiac phases	30
Time spacing (ms)	32.0
T_2^* (ms) [58]	254.0
ADC bandwidth (kHz) [55]	128.0
Slew-rate (mT/m/s) [56]	195.0
Max. gradient amplitude (mT/m) [56]	30.0

3.3. Computation and Comparison of Hemodynamic Parameters

In all the experiments conducted in this work, the primary focus is on comparing WSS, OSI, and \dot{E}_L [8, 25] parameters due to their dependence on blood viscosity. These parameters were estimated as follows:

$$\text{WSS}(\mathbf{x}, t) = \|\mathbf{l} \times \{(2\mu\dot{\boldsymbol{\varepsilon}}\mathbf{l}) \times \mathbf{l}\}\|_2, \quad \text{reported in Pascals} \quad (6a)$$

$$\text{OSI}(\mathbf{x}) = \frac{1}{2} \left(1 - \frac{\|\int_0^T \mathbf{l} \times \{(2\mu\dot{\boldsymbol{\varepsilon}}\mathbf{l}) \times \mathbf{l}\} dt\|_2}{\int_0^T \|\mathbf{l} \times \{(2\mu\dot{\boldsymbol{\varepsilon}}\mathbf{l}) \times \mathbf{l}\}\|_2 dt} \right), \quad \text{adimensional units} \quad (6b)$$

$$\dot{E}_L(\mathbf{x}, t) = 2\mu \left(\dot{\boldsymbol{\varepsilon}} - \frac{2}{3} \nabla \cdot \mathbf{u} \mathbf{I} \right) : \left(\dot{\boldsymbol{\varepsilon}} - \frac{2}{3} \nabla \cdot \mathbf{u} \mathbf{I} \right) V(\mathbf{x}), \quad \text{reported in micro-Watts} \quad (6c)$$

Here, \mathbf{l} denotes a unit inward surface normal vector, $2\mu\dot{\boldsymbol{\varepsilon}}\mathbf{l}$ represents the shear stress, T is the duration of the cardiac cycle, $V(\mathbf{x})$ is the Voronoi nodal volume distribution on the finite element mesh, and \mathbf{I} is the identity matrix. Additionally, $\|\cdot\|_2$ denotes the standard Euclidean vector norm. In the non-Newtonian case, the apparent viscosity varies both spatially and temporally, and this variation is accounted for by using μ_{PL} in the relevant expressions.

These three biomarkers were chosen because of their direct dependence on viscosity. The boundary layer near the vessel wall, influenced by blood rheology, can undergo thinning or thickening, which affects velocity gradients and, consequently, viscosity. In this context, evaluating WSS is crucial. OSI measures temporal changes in shear stress caused by variations in viscosity and flow dynamics, aspects not captured by t_{WSS} . Finally, \dot{E}_L quantifies how energy dissipates within the flow due to viscous fluid interactions, which are also sensitive to changes in viscosity.

To compare these three parameters, the aorta was divided into four segments: the ascending aorta (AAo, between the Valsalva level and the brachiocephalic trunk), the aortic arch (AArch, between the brachiocephalic trunk and the isthmus level), the proximal descending aorta (pDAo, between the isthmus level and the Valsalva level), and the distal descending aorta (dDAo, between the Valsalva level and the diaphragmatic level). This division into segments is not arbitrary and follows the anatomical references used in previous studies [5, 59, 60, 61, 1]. A schematic of these segments is shown in Figure 4. The mean values of WSS, OSI, and \dot{E}_L were then estimated for each segment to facilitate comparisons. In line with current practices [3, 62, 60, 63, 64], the supra-aortic branches (brachiocephalic, carotid, and subclavian arteries) were not included in the analysis due to the small number of voxels relative to artery diameters in this region, which affects the quantification of hemodynamic parameters.

The three quantities specified in (6) were estimated using the 4D Flow Matlab Toolbox [65], which employs a previously validated finite element scheme [66] to compute various hemodynamic and geometrical parameters from 4D Flow MRI data [1].

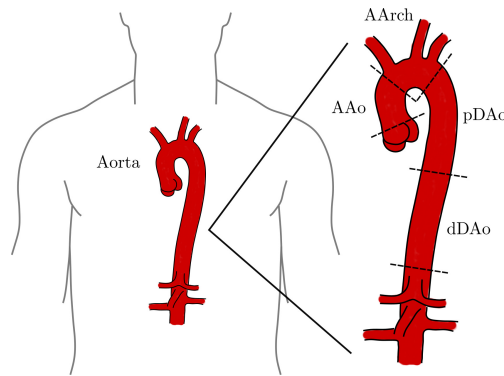


Figure 4: Aortic segments used for the quantification and comparison of hemodynamic parameters.

3.4. Experiment 1: evaluating the pertinence of the power-law

In this experiment, we aimed to assess whether Newtonian and non-Newtonian viscosity models yield equivalent results in terms of WSS, \dot{E}_L , and OSI across different Hct levels. The goal was to determine if a constant viscosity

model suffices to account for the effects of nonlinear viscosity on hemodynamic parameters. If the results between the models are similar, a constant viscosity would be deemed adequate. Otherwise, the adoption of a more complex model would be necessary.

To evaluate this, CFD simulations of a patient-specific aorta model (see Figure 1) were performed for the Hct values listed in Table 1, using both the fitted-Newtonian viscosities (μ_{NF}) and power-law viscosities (μ_{PL}) estimated as described in Section 2.4. Details of the model are provided in Section 3.1. The resulting velocity fields were then used to generate synthetic 4D Flow images as described in Section 2.3, which were processed to obtain WSS, \dot{E}_L , and OSI using both μ_{NF} and μ_{PL} accordingly. The procedure used to derive these parameters is detailed in Section 3.3.

To facilitate comparisons, mean and standard deviation values of all hemodynamic parameters within each segment, as described in Section 3.3, were computed at peak systole and diastole (see Figure 5). The reported values represent the average and standard deviation of the means across the four segments.

3.5. Experiment 2: comparison of current approaches with power-Law model parameter estimation

Given that blood exhibits shear-thinning behavior, this experiment aims to demonstrate the differences in the estimation of hemodynamic parameters when using a Newtonian viscosity (μ_N) compared to a model that accounts for shear-thinning behavior (μ_{PL}). To illustrate this, the same 4D Flow images generated in Experiment 1 from power-law viscosity CFD simulations were used to obtain WSS, \dot{E}_L , and OSI at different Hct levels. These parameters were estimated using both Newtonian viscosities within the typical range found in the literature and power-law viscosities as described in Section 2.4. It is important to note that the hemodynamic parameters estimated using the power-law model are exactly the same that those from Experiment 1.

Once again, to facilitate comparisons, mean and standard deviation values of all hemodynamic parameters within each segment, as described in Section 3.3, were computed at peak systole and diastole (see Figure 5). The reported values represent the average and standard deviation of the means across the four segments.

3.6. Experiment 3: in-vivo data

This experiment aims to replicate the results obtained in Experiment 2 using in-vivo data from patients with varying Hct levels, following the same processing procedure described previously. For this purpose, in-vivo gadolinium-enhanced triple-VENC 4D Flow images acquired from 5 patients with hypertrophic cardiomyopathy (2 males and 3 females, aged 68 ± 26 years) using a 3.0T Achieva scanner (Philips Healthcare, Best, The Netherlands) were used. These patient data are part of a larger dataset that has been previously utilized in [67] for the quantification of turbulent kinetic energy. The criterion used to choose the data was to have equispaced samples within the broadest Hct range possible. The imaging parameters included an acquired voxel size of $1.7 \times 1.7 \times 2.0$ mm³, VENCs of 50, 150, and 450 cm/s, a temporal resolution of 40 ms, and 15 to 21 frames depending on heart rate. Further details of the sequence and reconstruction can be found in [67].

Each patient had a Complete Blood Count (CBC) available, which is a comprehensive blood test that includes Hct measurement. Due to the use of gadolinium as a contrast agent, a kidney function test was required to determine its suitability. Therefore, blood tests were mandated within three months prior to imaging, which also included a complete blood count. The patients had Hct levels of 28.2, 35.2, 40.2, 46.6, and 50.1.

The experiments were conducted at Nippon Medical School Hospital, with the study approved by the Institutional Review Board. All subjects provided written informed consent.

4. Results

As described in Section 3.3, only the mean values across the four segments for each hemodynamic parameter, along with their respective standard deviations (representing variations across segments), are shown in this section to avoid visual clutter. Figures with detailed regional information for each segment are presented in Supplementary Figures S2 to S4.

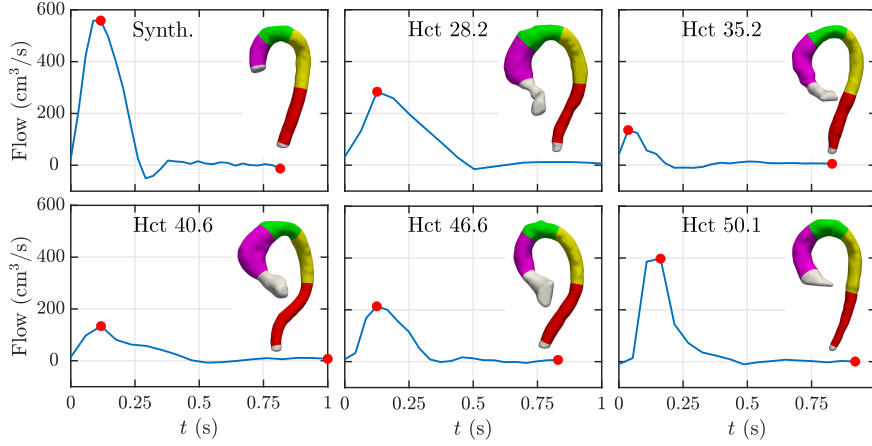


Figure 5: Flow curves obtained from 4D Flow images and the aortic segments considered in all analyses. The flow curves were measured at the ascending aorta, at the level of the pulmonary bifurcation. The top-left image shows the measurements from the synthetic dataset, while the remaining figures display the curves obtained from patient data.

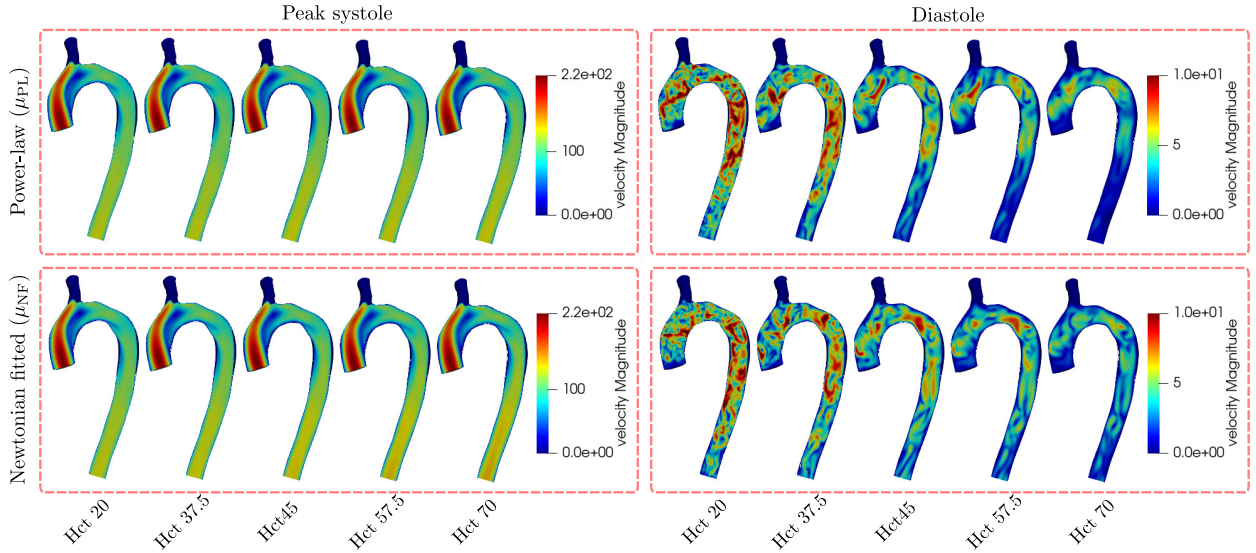


Figure 6: Velocity maps at peak systole and diastole, extracted from CFD simulations using power-law (μ_{PL}) and Newtonian-fitted (μ_{NF}) viscosities for different Hct values. Almost identical flow patterns are observed at peak systole, while some differences are noticeable at diastole, particularly in the descending aorta.

4.1. Experiment 1

Figure 6 shows the simulated velocities obtained using power-law (μ_{PL}) and fitted-Newtonian (μ_{NF}) viscosities. Both models produced nearly identical velocity profiles at peak systole across all Hct levels, while minor differences were observed in the descending aorta during diastole. Despite these differences, the overall flow dynamics between the two models also appear similar during diastole.

Despite the similarities in flow dynamics between the two models, Figure 7 shows that the hemodynamic parameters estimated from synthetic 4D Flow images exhibit noticeable differences at both systole and diastole. At systole, the average differences in WSS and \dot{E}_L across all Hct levels, relative to the power-law model, were $119.3 \pm 21.7\%$ and $61.8 \pm 14.4\%$, respectively. In absolute terms, these differences range from 0.458 to 2.883 Pa in WSS and from 0.089 to 0.911 μW for Hct values of 20 and 70, respectively. In all cases, the sign indicates whether the parameter estimated using fitted-Newtonian (μ_{NF}) viscosities was greater (positive) or smaller (negative) compared to the power-law estimations.

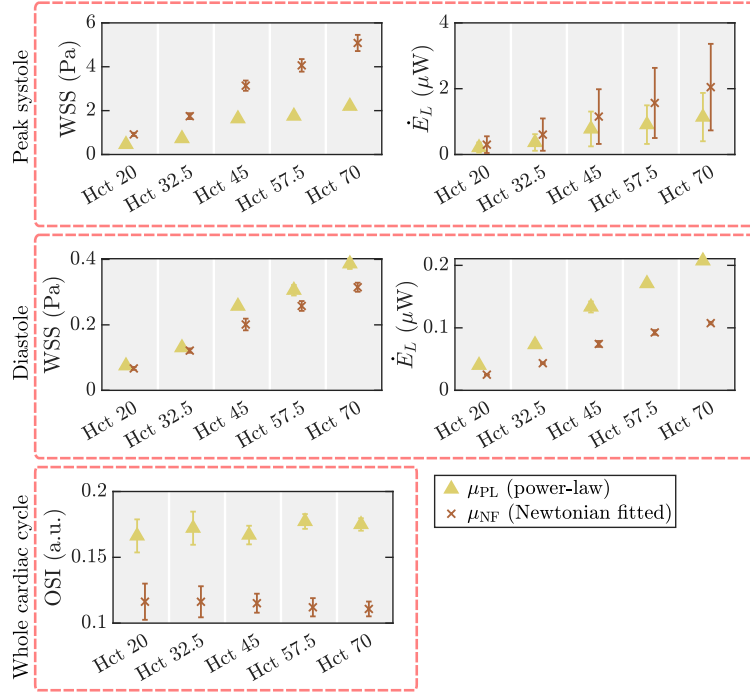


Figure 7: Mean values and standard deviations of WSS, OSI, and \dot{E}_L across four aortic segments were estimated from simulated images obtained from CFD simulations using power-law (μ_{PL}) and fitted-Newtonian (μ_{NF}) viscosities. The estimations were performed using viscosity models and values consistent with those used in the CFD simulations from which synthetic 4D Flow images were obtained. Clear differences were observed between the models for varying Hct values and cardiac phases, indicating that the two models cannot be used interchangeably.

In diastole, the differences observed in systole show inverted signs. The average differences in WSS and \dot{E}_L across all Hct levels were $-14.7 \pm 5.4\%$ and $-43.3 \pm 3.7\%$, respectively. In absolute terms, these differences range from -0.008 to -0.072 Pa in WSS and from -0.015 to -0.100 μW for Hct values of 20 and 70, respectively. Although the absolute differences are smaller, the relative differences and inverted signs suggest that using a Newtonian model for blood, even when adjusted by Hct level, is not suitable for capturing the nonlinear interactions of blood flow. Therefore, a Newtonian model cannot be used as a surrogate, justifying the inclusion of nonlinear rheology.

For OSI, the average difference across all Hct levels was $-33.4 \pm 2.8\%$. In absolute terms, the differences ranged from -0.050 to -0.064 for Hct values of 20 and 70, respectively. Since OSI is a metric calculated over the entire cardiac cycle, the negative sign indicates that the WSS vector experienced greater variation when the blood exhibited nonlinear behavior, consistent with our findings stated in previous paragraphs.

Additionally, greater variability between segments was observed in \dot{E}_L at peak systole compared to WSS and OSI (see Figure 7). This is more clearly illustrated in Figure A.1 in Appendix A, which shows the means and standard deviations of hemodynamic parameters within each aortic segment. Higher values were found in the ascending aorta, primarily due to the flow dynamics (see Figure 6).

Finally, Figure 8 shows the WSS calculated directly from the FE simulations using both models at peak systole and diastole. The same trends in differences are observed in these simulations as those obtained from the synthetic 4D Flow MR images.

4.2. Experiment 2

Given that blood exhibits shear-thinning behavior, Figure 9 shows the hemodynamic parameters estimated from synthetic 4D Flow images generated from simulations with a power-law blood rheology. The parameters were estimated using both power-law (μ_{PL}) and standard Newtonian (μ_N) viscosities commonly found in the literature. At systole, the differences in WSS and \dot{E}_L across all Hct levels (relative to the power-law model and using $\mu_N = 0.0035$ Pa \cdot s as reference) ranged from 189.4% to -41.3% and from 112.9% to -60.4% for Hct values of 20 and 70, respectively.

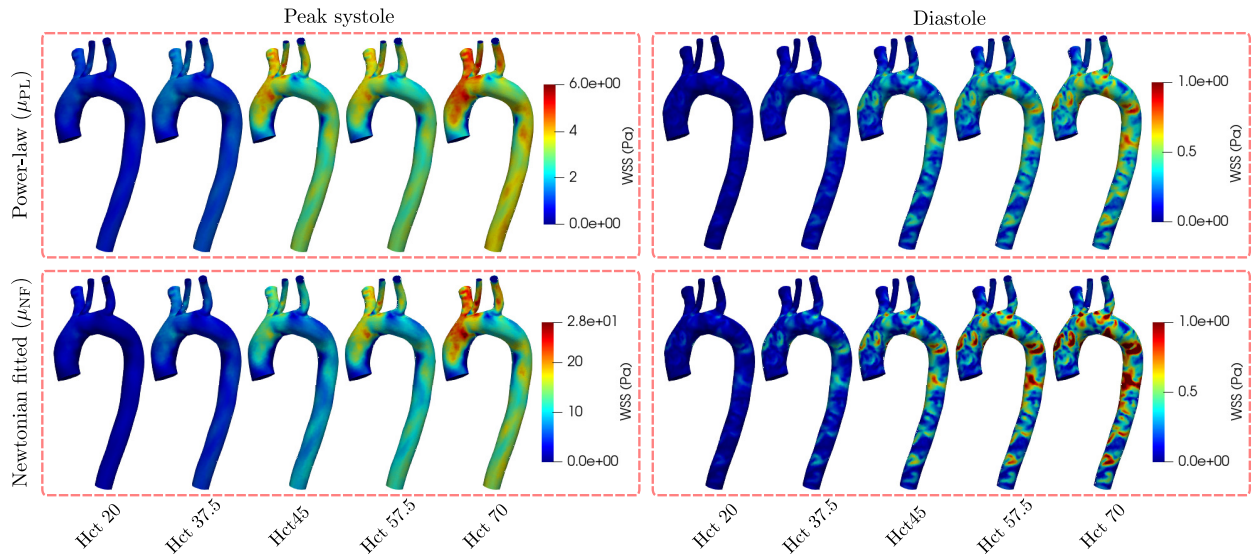


Figure 8: WSS maps at peak systole and diastole were estimated from CFD simulations using power-law (μ_{PL}) and fitted-Newtonian (μ_{NF}) viscosities for different Hct values. The WSS obtained from the fitted-Newtonian simulations is greater at peak systole but smaller at diastole compared to those obtained using the power-law model, indicating that the two simulations cannot be used interchangeably.

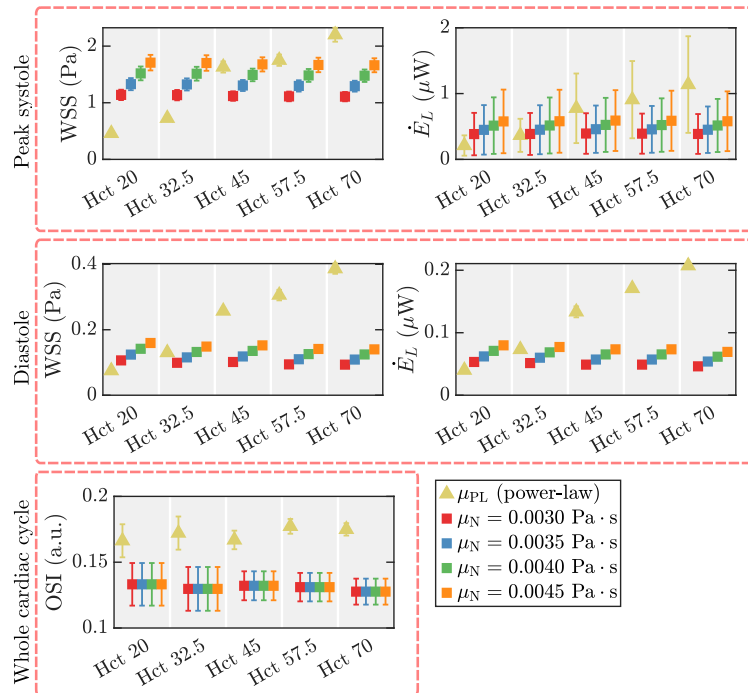


Figure 9: Mean values and standard deviations of WSS, OSI, and \dot{E}_L across four aortic segments were estimated from synthetic 4D Flow images generated by CFD simulations using power-law viscosities. Hemodynamic parameters were estimated using both power-law (μ_{PL}) and state-of-the-art Newtonian (μ_N) viscosities. Clear differences were observed between the models across varying Hct values and cardiac phases, indicating that the choice of viscosity model can lead to significant discrepancies in hemodynamic parameter estimations.

In absolute terms, these differences ranged from 0.870 to -0.908 Pa for WSS and from 0.238 to -0.686 μW for Hct values of 20 and 70, respectively. The sign change indicates that WSS and \dot{E}_L estimated using Newtonian viscosities can be either greater (positive) or smaller (negative) than the power-law estimations, depending on the Hct level.

These differences can be better observed in Figure 10 for WSS maps obtained on the segmented aorta at peak systole.

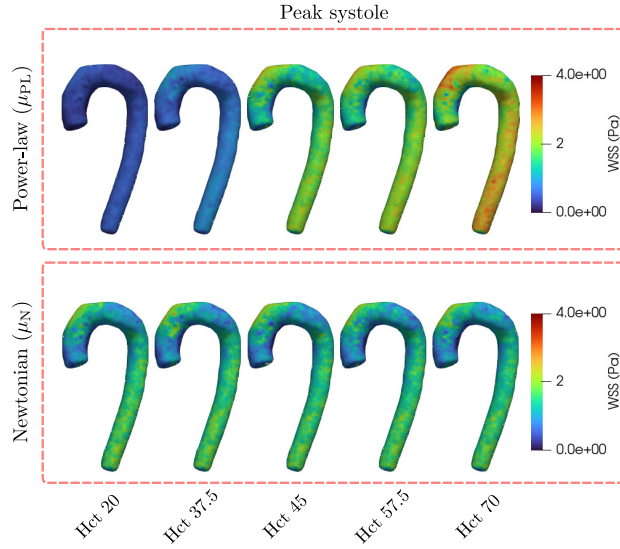


Figure 10: WSS maps at peak systole estimated from synthetic 4D Flow images generated by CFD simulations using power-law viscosities. The estimations shown were obtained using power-law (μ_{PL}) viscosities and a Newtonian viscosity of $\mu_N = 0.0035 \text{ Pa} \cdot \text{s}$.

In diastole, the results were similar, with relative differences in WSS ranging from 65.5% to -71.8% (using $\mu_N = 0.0035 \text{ Pa} \cdot \text{s}$ as reference) and from 54.9% to -74.0% in \dot{E}_L at peak systole. However, during this cardiac phase, the sign change for WSS occurs at an Hct of 32.5, which is earlier than at peak systole. In absolute terms, these differences ranged from 0.0491 to -0.278 Pa for WSS and from 0.022 to $-0.153 \mu\text{W}$ for Hct values of 20 and 70, respectively. These differences can be better observed in Figure 11 for WSS maps obtained on the segmented aorta at diastole.

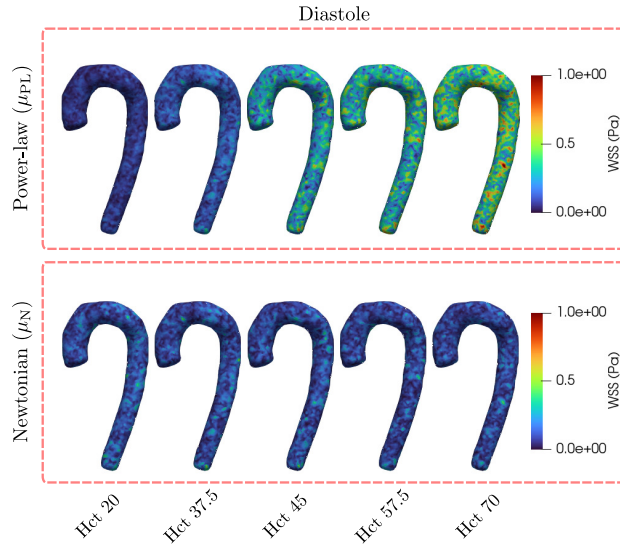


Figure 11: WSS maps at diastole estimated from synthetic 4D Flow images generated by CFD simulations using power-law viscosities. The estimations shown were obtained using power-law (μ_{PL}) viscosities and a Newtonian viscosity of $\mu_N = 0.0035 \text{ Pa} \cdot \text{s}$.

For OSI, higher values were obtained using constant Newtonian viscosities (μ_N) from images generated by power-law simulations, compared to those obtained with fitted-Newtonian viscosities (μ_{NF}) in Experiment 1 (see Figures 7

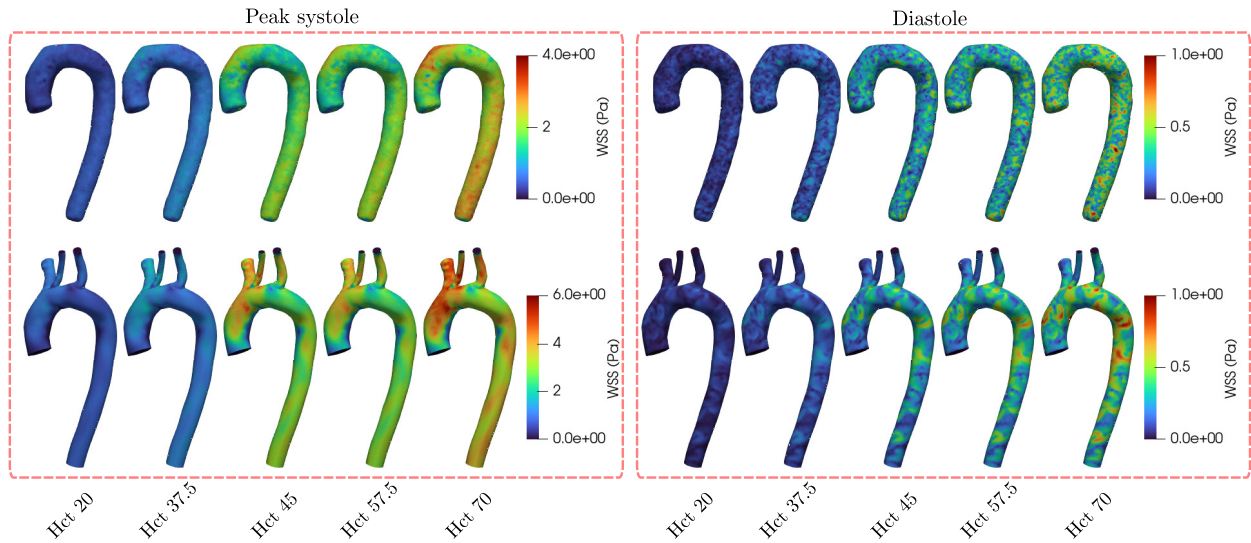


Figure 12: WSS maps at peak systole and diastole estimated from synthetic 4D Flow images generated by CFD simulations using power-law viscosities. The color bars at peak systole have different ranges to clearly display the spatial distributions. The results reveal similar spatial variations in WSS between the images and simulations, despite the presence of noise, partial volume effects, and flow artifacts, at both peak systole and diastole. However, consistent with previous reports in the literature, WSS values estimated from 4D Flow images tend to underestimate those obtained from simulations.

and 9). This can be attributed to variations in flow dynamics between the linear and nonlinear rheology models, which are not apparent in the overall flow pattern showed in Figure 6 but significantly affect the velocity gradients near the vessel walls. Using $\mu_N = 0.0035 \text{ Pa} \cdot \text{s}$ as reference, the relative differences with respect to the power-law estimations ranged from -19.9% to -27.0% for Hct values of 20 and 70, respectively. In absolute terms, the differences ranged from -0.033 to -0.047 for the same Hct range. Again, the negative sign indicates that the WSS vector experienced greater temporal variations when the blood exhibited a nonlinear behavior.

Similar to the results in Experiment 2, greater variability between segments was observed in \dot{E}_L at peak systole compared to WSS and OSI (see Figure 9). This is more clearly illustrated in Figure A.2 in Appendix A, which shows the means and standard deviations of hemodynamic parameters within each aortic segment.

Since we have shown differences at peak systole and diastole between estimations made using both viscosity models (μ_N and μ_{PL}), it is important to determine whether the parameters estimated using the power-law model are consistent with the simulations. These similarities are highlighted in Figure 8, which shows that the WSS maps estimated from images and CFD simulations exhibit similar spatial variations. However, smaller WSS values were found at peak systole from synthetic 4D Flow MR images compared to their simulation counterparts, with differences around 40% of the CFD simulation values. At diastole, the same WSS values were observed, but the estimations obtained from images were highly affected by noise.

4.3. Experiment 3

Figure 13 shows the hemodynamic parameters estimated from in-vivo 4D Flow MR images. It should be noted that the Hct range in this experiment differs from that in Experiments 1 and 2, ranging from 28.2 to 50.1, compared to 20 to 70 in the previous experiments. Additionally, the Hct values in this case are not equispaced. As evident from the figure, using the power-law viscosity (μ_{PL}) for estimating hemodynamic parameters resulted in greater values in almost all cases. The only instance where WSS and \dot{E}_L were smaller was at an Hct of 28.2 during peak systole.

At peak systole, for an Hct of 28.2 (the lowest), the relative differences with respect to the power-law estimation (using $\mu_N = 0.0035 \text{ Pa} \cdot \text{s}$ as a reference) were 41.4% in WSS and 1.5% in \dot{E}_L . For an Hct of 50.1 (the highest), the differences were -21.0% and -45.4% , respectively. However, the largest differences were observed at an Hct of 46.6, with -45.0% in WSS and -60.4% in \dot{E}_L . In absolute terms, these differences in WSS and \dot{E}_L were 0.125 Pa and 0.001 μW , -0.543 Pa and $-0.101 \mu\text{W}$, and -0.312 Pa and $-0.081 \mu\text{W}$ for Hct levels of 28.2, 50.1, and 46.6, respectively.

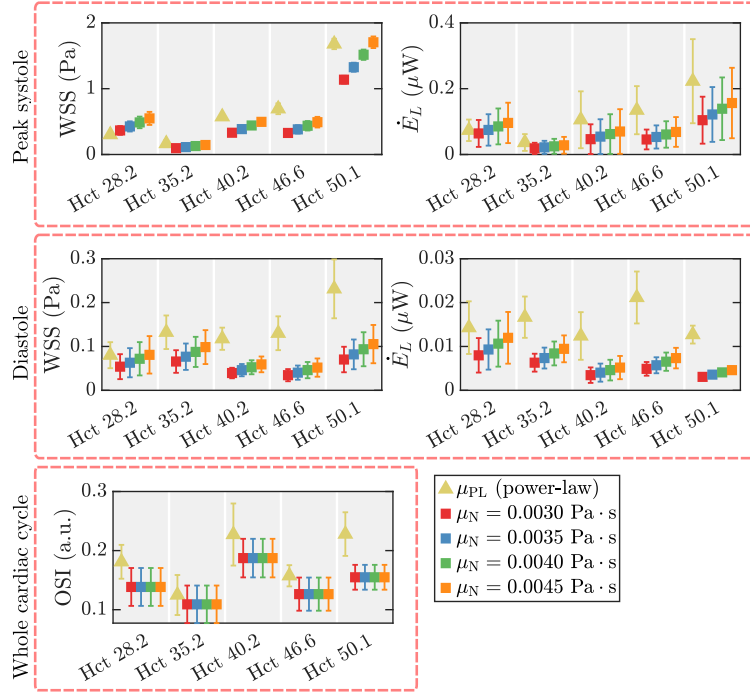


Figure 13: Mean values and standard deviations of WSS, OSI, and \dot{E}_L across four aortic segments were estimated from in-vivo 4D Flow images of HCM patients. Hemodynamic parameters were estimated using both power-law (μ_{PL}) and state-of-the-art Newtonian (μ_N) viscosities. Clear differences were observed between the models across varying Hct values and cardiac phases, indicating that the choice of viscosity model can lead to significant discrepancies in hemodynamic parameter estimations.

In diastole, these differences become larger. For an Hct of 28.2, the relative differences were -21.4% in WSS and -34.8% in \dot{E}_L , while for an Hct of 50.1, they were -64.6% and -71.8% , respectively. However, as with the peak-systolic results, the largest differences were observed at an Hct of 46.6, with -69.0% in WSS and 73.0% in \dot{E}_L . In absolute terms, these differences in WSS and \dot{E}_L were -0.017 Pa and -0.005 μW , -0.149 Pa and -0.009 μW , and -0.090 Pa and -0.016 μW for Hct levels of 28.2, 50.1, and 46.6, respectively.

For OSI, the relative differences with respect to the power-law estimations averaged $-21.1 \pm 6.5\%$ (\pm one standard deviation) across all Hct values considered in the experiment. In absolute terms, this variation averaged -0.041 ± 0.019 . These results indicate that using μ_{PL} to estimate WSS reveals greater temporal variations, consistent with the findings from Experiment 2.

Although smaller differences between models were found in the in-vivo data, this can be explained by the different blood dynamics and lower flows observed at peak systole compared to the CFD simulations (see Figure 5). The reduced flow likely generates smaller velocity gradients near the vessel walls, leading to lower estimations of WSS and \dot{E}_L . OSI, on the other hand, is a parameter normalized with respect to time, which helps to maintain the observed differences.

Finally, Figures 14 and 15 show the WSS maps estimated from each patient's data at peak systole and diastole, respectively. The differences described in the previous paragraphs are clearly illustrated in these figures. Additionally, readers are referred to Figure A.3 in Appendix A for the means and standard deviations of WSS, E_L , and OSI within each aortic segment.

5. Discussion

Experiment 1 tested the necessity of a non-Newtonian model when computing key parameters such as those defined in (6). The significance of both experiments lies in assessing whether the Newtonian linear model (μ_{NF}) could

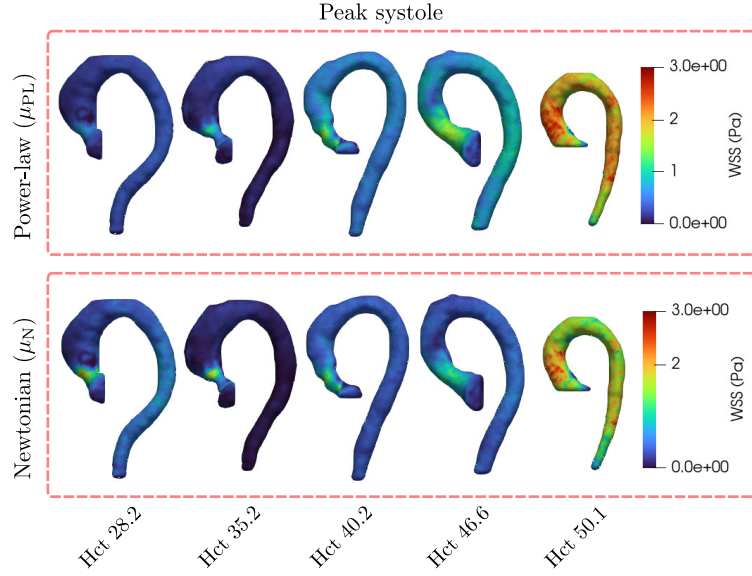


Figure 14: WSS maps at peak systole estimated from in-vivo 4D Flow images of patients with HCM at different Hct levels. The estimations shown were obtained using power-law (μ_{PL}) viscosities and a Newtonian viscosity of $\mu_N = 0.0035 \text{ Pa} \cdot \text{s}$.

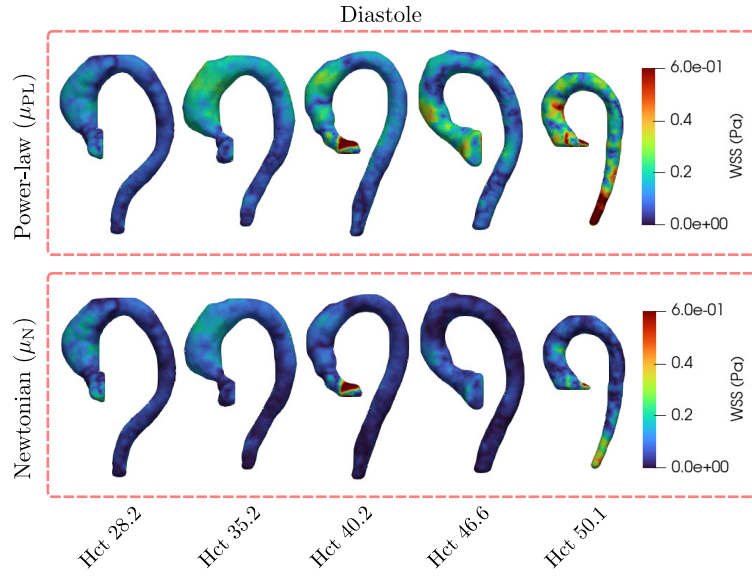


Figure 15: WSS maps at diastole estimated from in-vivo 4D Flow images of patients with HCM at different Hct levels. The estimations shown were obtained using power-law (μ_{PL}) viscosities and a Newtonian viscosity of $\mu_N = 0.0035 \text{ Pa} \cdot \text{s}$.

serve as a surrogate for the power-law constitutive model, thus eliminating the need to account for nonlinear rheology. However, the differences observed in Figure 7 indicate that the two models are neither interchangeable, similar, nor equivalent. These differences reached up to 120% in some cases. These results suggests that, given the well-established shear-thinning behavior of blood in the literature, a constant viscosity model is insufficient for estimating hemodynamic parameters. The flow dynamics cannot be accurately characterized using a constant viscosity, underscoring the need to consider nonlinear models.

Since we have established the necessity of accounting for the nonlinear behavior of blood, Experiment 2 evaluated the extent of the differences in WSS, \dot{E}_L , and OSI when using an incorrect (but usually employed), model—specifically, Newtonian (constant) viscosities (μ_N)—compared to the power-law viscosity model (μ_{PL}). Results showed significant

differences between the estimations made with the two models (see Figures 9, 10, and 11), highlighting that using a constant viscosity model can lead to inaccurate predictions of hemodynamic parameters when nonlinear blood rheology is present. This was further confirmed in Figure 8, where WSS maps estimated from 4D Flow images demonstrated similar spatial distributions and Hct-level variations compared to their CFD simulation counterparts, though significant underestimations were observed at peak systole.

However, the underestimation found at peak systole aligns with previous studies, which indicate that hemodynamic parameters, particularly WSS, are consistently underestimated when using 4D Flow MRI [68, 69, 66, 70, 71, 72, 64, 63]. Moreover, we observed the same behavior reported in [72] and [63]: WSS is significantly underestimated during systole (around 40% in our case), and these differences diminish during diastole. These findings provide confidence that all estimations made from images are faithful representations of the ground-truth estimations derived from CFD simulations.

Up to this point, it is important to acknowledge that Experiments 1 and 2 were conducted using only one geometry from a healthy volunteer under various viscosity scenarios. However, we believe that the conclusions discussed in the previous paragraphs remain valid due to the way we formulated our research questions. Firstly, we aimed to determine whether using a linear viscosity model could yield equivalent results to those obtained with a nonlinear rheology. Secondly, if the answer to the first question was negative, we sought to quantify the differences when considering the nonlinear rheology of blood versus the current standard approach. Therefore, to answer both questions, presenting one counterexample is sufficient.

Hemodynamic parameters obtained from in-vivo data in Experiment 3 also exhibited notable differences compared to the results obtained in experiments 1 and 2. However, despite the insightful and promising results, their interpretation must be carefully approached. This is due to several reasons: first, the limited number of data points (five) is insufficient for claiming definitive trends. Second, the range of Hct considered in the in-vivo experiments is smaller than that considered in the simulations (28.2 to 50.1 versus 20 to 70, respectively), and third, the data was obtained from patients with different types of HCM. Therefore, it is a future endeavor of the authors to extend this study to a larger population, including healthy volunteers and patients with various diseases, to obtain trends and statistics that would be clinically meaningful.

The observed differences between estimations using the power-law (μ_{PL}) and Newtonian (μ_N) viscosities are noteworthy and warrant discussion. As highlighted earlier, hemodynamic parameters are often underestimated in 4D Flow MRI due to resolution-related imaging effects, particularly partial volume effects. This underestimation can be substantial, exceeding 50% of the ground-truth value during systole for a pixel size of 2 mm [63]. It could be argued that such underestimations might influence the differences observed in this investigation. However, it is important to recognize that these underestimations are inherent in all 4D Flow-derived hemodynamic parameters. Despite this limitation, our study still revealed significant differences and consistent hemodynamic parameters when compared to CFD simulations.

Regarding the current approach to estimating hemodynamic parameters, it is important to note that the high variability in Newtonian viscosity values reported in the literature could introduce bias into the statistics of viscosity-dependent parameters, potentially limiting their diagnostic utility. Therefore, using a measurable criterion such as Hct to standardize the estimation of hemodynamic parameters would represent a significant improvement. In this context, we believe that introducing a simple shear-thinning viscosity model, such as the power-law, could enhance the accuracy of viscosity-dependent hemodynamic parameter estimation, ultimately leading to a better understanding of cardiovascular diseases.

Having said that, it is important to note that this investigation focused solely on the use of the power-law model. Other viscosity models, such as the Carreau-like [13, 14, 15], Cross [16, 12], and Casson models [17], were not considered. However, as shown in the literature, the power-law model has provided similar results in terms of flow dynamics and hemodynamic parameters when compared to other models in vessels such as the coronary arteries and the aorta [73, 74]. It remains unclear whether it would be possible to differentiate between these models using 4D Flow MRI measurements due to the presence of partial volume effects, flow artifacts, and noise.

A limitation of this investigation is the lack of readily available power-law parameters for a wide range of Hct levels at physiological temperature (e.g., 37°C). In most of the literature reviewed for this work, only graphical representations of the adjusted curves were provided, making the task of extracting the values of m and n complicated. This challenge led to the development of the methodology used in this study to calculate these values for any Hct level within the range of 20 to 70 (as described in Section 2.4) based on discrete Hct data from a single article [18].

This limitation underscores the need for standardizing blood rheology research by providing both the parameters of the adjusted models and the corresponding measurements.

All previous experiments and discussions assumed that the Hct level is known for every patient at the time of the 4D Flow exam. While this assumption may not always hold, it is reasonable to expect that, in most cases, this data will be available, as CBCs are routinely performed in patients with heart failure and related comorbidities [75]. Additionally, CMR exams often use gadolinium contrast agents, which are contraindicated in patients with severe renal impairment, necessitating a CBC to assess renal function. Furthermore, this assumption is even more plausible considering that CMR exams are typically conducted later in the diagnostic process, primarily due to their higher cost. However, this raises a related question: is the CBC still valid at the time of the 4D Flow exam?

Many efforts have been made to address this question in various contexts, including MRI. For instance, studies have shown that not only Hct but also several other hematological parameters can vary with posture [76], throughout the day [77, 78], and seasonally [79, 80, 81]. Other sources of variability include pre-analytical factors such as fasting condition, venous stasis, and exercise, which are usually standardized to reduce variation [81].

Considering these factors, the reported variations in Hct have been demonstrated not to affect the estimation of CMR-derived parameters directly dependent on Hct, such as extracellular volume [82]. Thus, we hypothesize that these variations would not induce significant differences in hemodynamic parameters estimated from 4D Flow data. However, this remains an open question.

6. Conclusion

Our study highlights the importance of accounting for the nonlinear behavior of blood when estimating hemodynamic parameters from 4D Flow MRI using available CBC data. The conventional use of Newtonian or fitted-Newtonian viscosities is insufficient for capturing the complex dynamics of blood flow, particularly in major vessels like the aorta. This research shows that using the simple power-law model as the ground truth leads to significant differences in both simulations and synthetic 4D Flow MRI data compared to linear Newtonian (or fitted-Newtonian) models. These differences, across a wide range of Hct values, can be as high as 190% and 113% in WSS and \dot{E}_L at systole, and as low as -72% and -74% at diastole, respectively. In in-vivo data, differences in WSS and \dot{E}_L can reach up to -45% and -60% at systole, and range from -69% to 73% at diastole.

A key limitation is the lack of readily available power-law parameters for a wide range of Hct levels under physiological conditions. This highlights the need for future research to develop comprehensive databases of power-law parameters, as well as other rheological models, across different Hct values. Such databases would improve the accuracy of hemodynamic parameter estimations and contribute to the standardization of blood rheology research. In this regard, the methodology described in Section 2.4 is freely available at github.com/hmella/power-law-parameters.

Future work will focus on four main areas. First, we will explore the potential of blood viscosity maps as biomarkers by investigating the spatial distribution of viscosity in the cardiovascular system and its correlation with disease-related changes. Second, we will assess the impact of timely Hct measurements on the estimation of hemodynamic parameters. Third, we will conduct a statistical analysis across a wide range of Hct values to evaluate the robustness and clinical applicability of the proposed model in both volunteers and patients. Finally, we will investigate the use of other rheological models, such as Carreau-like, Cross, and Casson, for the estimation of hemodynamic parameters.

7. Acknowledgments

HM, JS, and EC acknowledge the financial support given by ANID-Fondecyt through the projects *Iniciación en Investigación* #11241098 and #11200481, and *Regular* #1210156, respectively. JS also acknowledges to ANID-Millennium Science Initiative Program ICN2021_004. FG acknowledges the funding PUCV Vinci DI-Iniciación 039.482/2024. We would like to kindly thank the Weierstraß-Institut für Angewandte Analysis und Stochastik (WIAS) for allowing the authors to run CFD simulations in their servers.

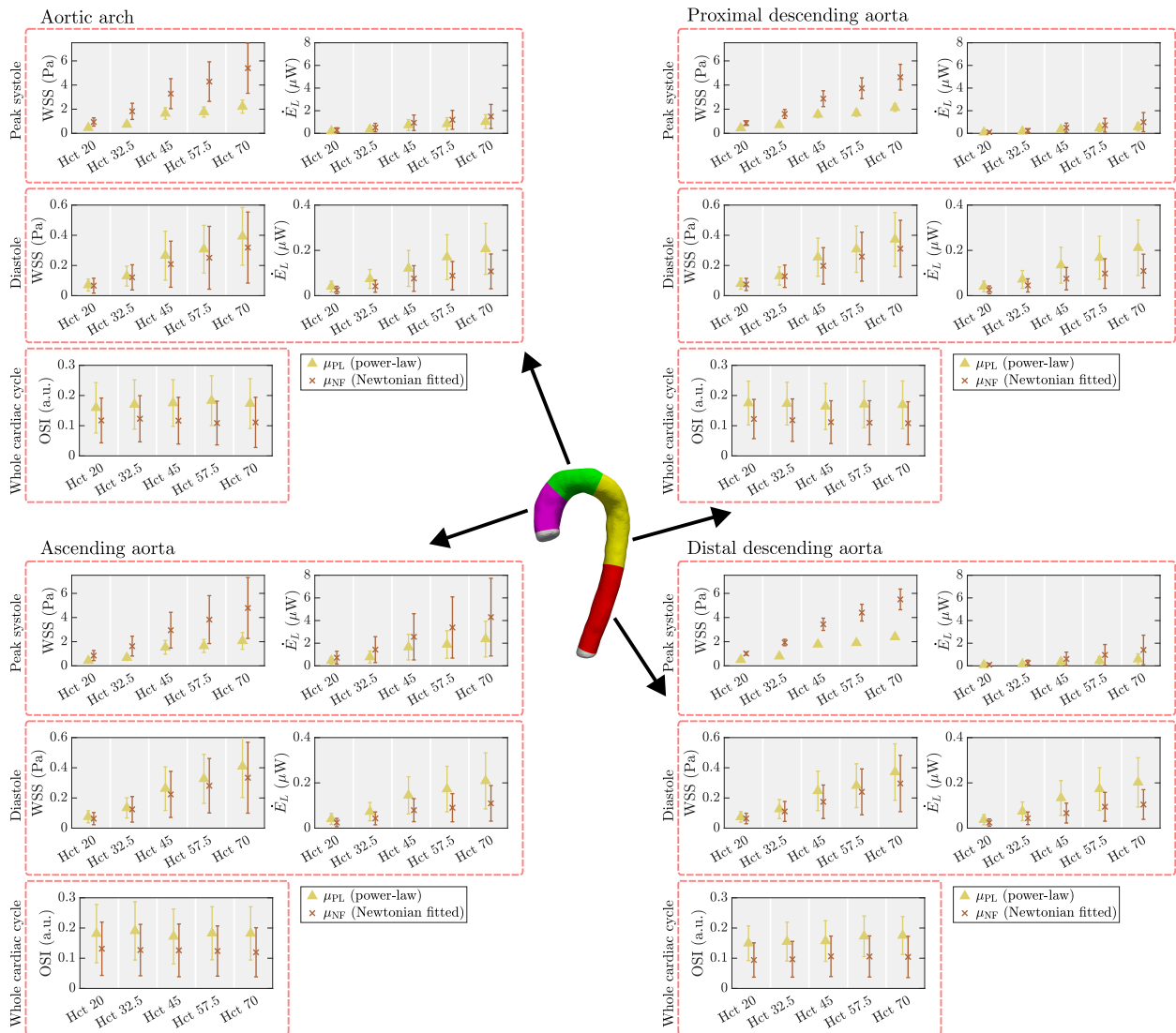


Figure A.1: Mean values and standard deviations of WSS, \dot{E}_L , and OSI within each aortic segment, estimated from simulated 4D Flow images generated from CFD simulations using power-law (μ_{PL}) and fitted-Newtonian (μ_{NF}) viscosities. The estimations were performed using viscosity models and values consistent with those used in the CFD simulations that generated the synthetic 4D Flow images. Results are presented for both peak systole and diastole. Higher values and greater variability are observed in the ascending aorta due to the flow dynamics. The same differences shown in Figure 7 are clearly depicted here for each segment.

Appendix A. Hemodynamic parameters for each aortic segments

References

- [1] J. Sotelo, P. Franco, A. Guala, L. Dux-Santoy, A. Ruiz-Muñoz, A. Evangelista, H. Mella, J. Mura, D. E. Hurtado, J. F. Rodríguez-Palomares, S. Uribe, Fully Three-Dimensional Hemodynamic Characterization of Altered Blood Flow in Bicuspid Aortic Valve Patients With Respect to Aortic Dilatation: A Finite Element Approach, *Frontiers in Cardiovascular Medicine* 9 (2022).
- [2] J. F. Jr. LaDisa, R. J. Dholakia, C. A. Figueroa, I. E. Vignon-Clementel, F. P. Chan, M. M. Samyn, J. R. Cava, C. A. Taylor, J. A. Feinstein, Computational simulations demonstrate altered wall shear stress in aortic coarctation patients treated by resection with end-to-end anastomosis, *Congenital Heart Disease* 6 (5) (2011) 432–443. doi : 10.1111/j.1747-0803.2011.00553.x.
- [3] E. S. Farag, P. van Ooij, R. N. Planken, K. C. Dukker, F. de Heer, B. J. Bouma, D. Robbers-Visser, M. Groenink, A. J. Nederveen, B. A. de Mol, J. Kluin, S. M. Boekholdt, Aortic valve stenosis and aortic diameters determine the extent of increased wall shear stress in bicuspid aortic valve disease, *Journal of Magnetic Resonance Imaging* 48 (2) (2018) 522–530. doi : 10.1002/jmri.25956.

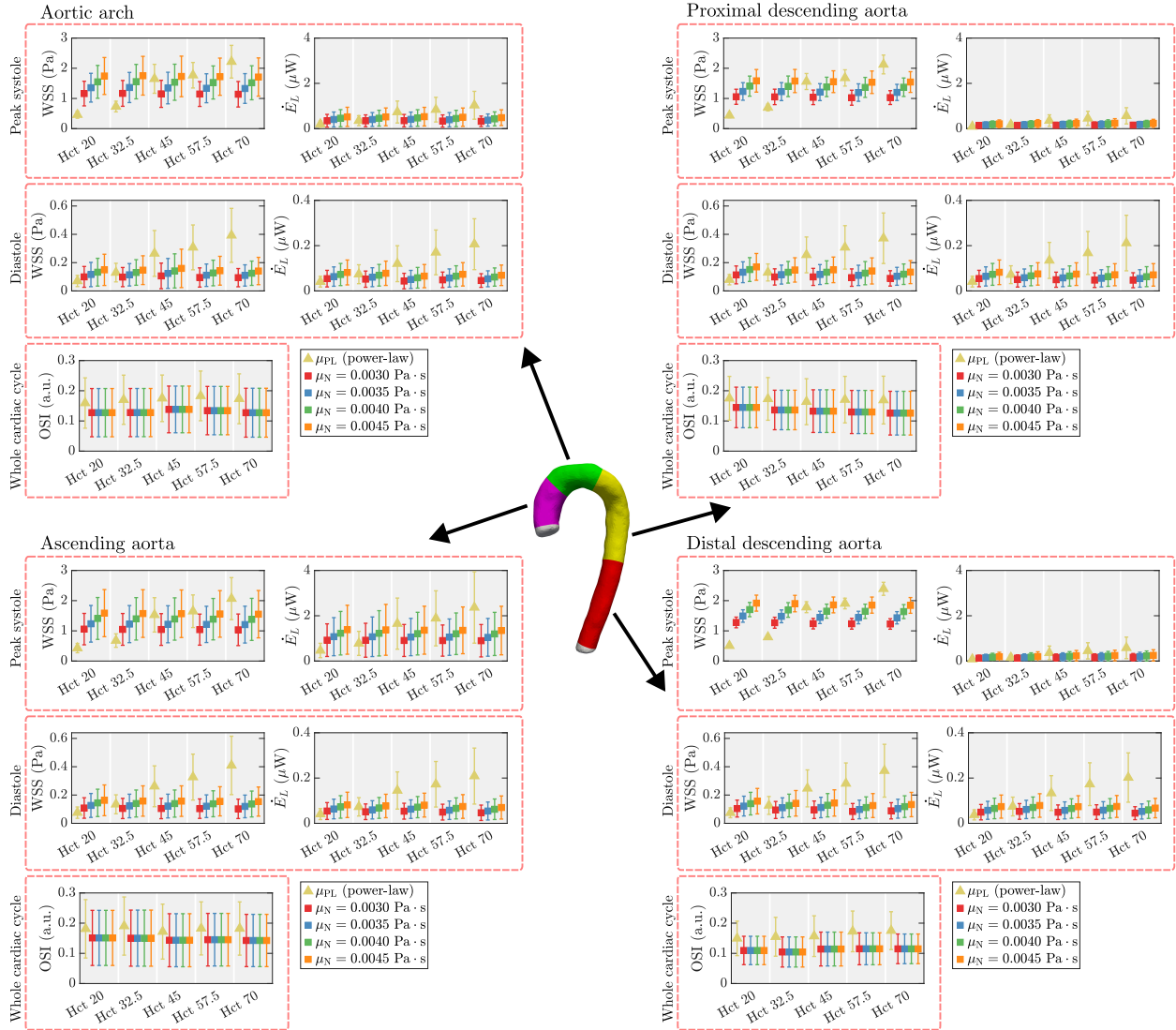


Figure A.2: Mean values and standard deviations of WSS, OSI, and \dot{E}_L within each aortic segment estimated from synthetic 4D Flow images generated by CFD simulations obtained using power-law viscosities. Hemodynamic parameters were estimated using both power-law (μ_{PL}) and state-of-the-art Newtonian (μ_N) viscosities. Results are presented for both peak systole and diastole. Higher values and greater variability are observed in the ascending aorta due to the flow dynamics. The same differences shown in Figure 9 are clearly depicted here for each segment.

- [4] K. Takahashi, T. Sekine, T. Ando, Y. Ishii, S. Kumita, Utility of 4d flow mri in thoracic aortic diseases: A literature review of clinical applications and current evidence, *Magn Reson Med Sci* 21 (2) (2021) 327–339. doi:10.2463/mrms.rev.2021-0046.
- [5] A. Harloff, A. Nußbaumer, S. Bauer, A. F. Stalder, A. Frydrychowicz, C. Weiller, J. Hennig, M. Markl, In vivo assessment of wall shear stress in the atherosclerotic aorta using flow-sensitive 4D MRI, *Magnetic Resonance in Medicine* 63 (6) (2010) 1529–1536. doi:10.1002/mrm.22383.
- [6] E. T. Biegling, A. Frydrychowicz, A. Wentland, B. R. Landgraf, K. M. Johnson, O. Wieben, C. J. François, In vivo three-dimensional MR wall shear stress estimation in ascending aortic dilatation, *Journal of Magnetic Resonance Imaging* 33 (3) (2011) 589–597. doi:10.1002/jmri.22485.
- [7] P. van Ooij, W. V. Potters, A. Guédon, J. J. Schneiders, H. A. Marquering, C. B. Majoie, E. vanBavel, A. J. Nederveen, Wall shear stress estimated with phase contrast MRI in an in vitro and in vivo intracranial aneurysm, *Journal of Magnetic Resonance Imaging* 38 (4) (2013) 876–884. doi:10.1002/jmri.24051.
- [8] A. Barker, P. van Ooij, K. Bandi, J. Garcia, M. Albaghdadi, P. McCarthy, R. Bonow, J. Carr, J. Collins, S. Malaisrie, M. Markl, Viscous energy loss in the presence of abnormal aortic flow, *Magn Reson Med* 72 (3) (2014) 620–628. doi:10.1002/mrm.24962.
- [9] J. Garay, H. Mella, J. Sotelo, C. Cárcamo, S. Uribe, C. Bertoglio, J. Mura, Assessment of 4D flow MRI's quality by verifying its Navier–Stokes

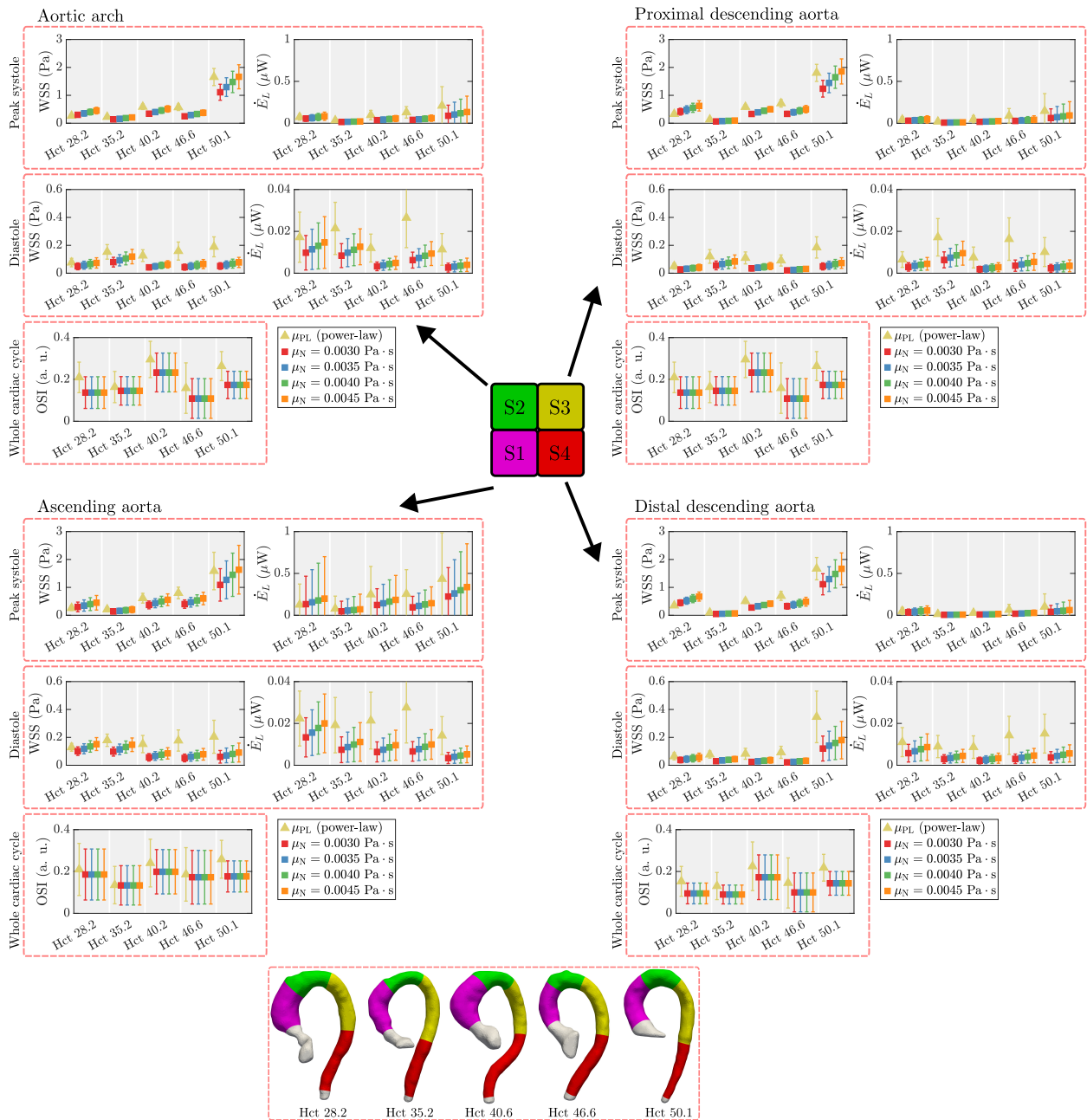


Figure A.3: Mean values and standard deviations of WSS, OSI, and \dot{E}_L within each aortic segment estimated from in-vivo 4D Flow images of HCM patients. Hemodynamic parameters were estimated using both power-law (μ_{PL}) and state-of-the-art Newtonian (μ_N) viscosities. Results are presented for both peak systole and diastole. Higher values and greater variability are observed in the ascending aorta due to the flow dynamics. The same differences shown in Figure 13 are clearly depicted here for each segment.

compatibility, International Journal for Numerical Methods in Biomedical Engineering 38 (6) (2022) e3603. doi:10.1002/cnm.3603.

[10] R. J. van Tuijl, K. M. Timmins, B. K. Velthuis, P. van Ooij, J. J. Zwanenburg, Y. M. Ruijgrok, I. C. van der Schaaf, Hemodynamic Parameters in the Parent Arteries of Unruptured Intracranial Aneurysms Depend on Aneurysm Size and Are Different Compared to Contralateral Arteries: A 7 Tesla 4D Flow MRI Study, Journal of Magnetic Resonance Imaging 59 (1) (2024) 223–230. doi:10.1002/jmri.28756.

[11] P. K. Mandal, An unsteady analysis of non-Newtonian blood flow through tapered arteries with a stenosis, International Journal of Non-Linear Mechanics 40 (1) (2005) 151–164. doi:10.1016/j.ijnonlinmec.2004.07.007.

[12] J. B. Mendieta, D. Fontanarosa, J. Wang, P. K. Paritala, T. McGahan, T. Lloyd, Z. Li, The importance of blood rheology in patient-specific

- computational fluid dynamics simulation of stenotic carotid arteries, *Biomechanics and Modeling in Mechanobiology* 19 (5) (2020) 1477–1490. doi:10.1007/s10237-019-01282-7.
- [13] F. M. Box, R. J. Van Der Geest, M. C. Rutten, J. H. Reiber, The influence of flow, vessel diameter, and non-Newtonian blood viscosity on the wall shear stress in a carotid bifurcation model for unsteady flow, *Investigative Radiology* 40 (5) (2005) 277–294. doi:10.1097/01.rli.0000160550.95547.22.
- [14] S. W. Lee, D. A. Steinman, On the relative importance of rheology for image-based CFD models of the carotid bifurcation, *Journal of Biomechanical Engineering* 129 (2) (2007) 273–278. doi:10.1115/1.2540836.
- [15] H. Gharahi, B. A. Zambrano, D. C. Zhu, J. K. DeMarco, S. Baek, Computational fluid dynamic simulation of human carotid artery bifurcation based on anatomy and volumetric blood flow rate measured with magnetic resonance imaging, *International Journal of Advances in Engineering Sciences and Applied Mathematics* 8 (1) (2016) 46–60. doi:10.1007/s12572-016-0161-6.
- [16] C. Abugattas, A. Aguirre, E. Castillo, M. Cruchaga, Numerical study of bifurcation blood flows using three different non-Newtonian constitutive models, *Applied Mathematical Modelling* 88 (2020) 529–549. doi:10.1016/j.apm.2020.06.066.
- [17] T. Suzuki, H. Takao, T. Suzuki, S. Hataoka, T. Kodama, K. Aoki, K. Otani, T. Ishibashi, H. Yamamoto, Y. Murayama, M. Yamamoto, Proposal of hematocrit-based non-Newtonian viscosity model and its significance in intracranial aneurysm blood flow simulation, *Journal of Non-Newtonian Fluid Mechanics* 290 (February) (2021) 1–11. doi:10.1016/j.jnnfm.2021.104511.
- [18] R. E. Wells, E. W. Merrill, Influence of flow properties upon viscosity-hematocrit relationships, *The Journal of Clinical Investigation* 41 (8) (1962) 1591–1598. doi:10.1172/JCI104617.
- [19] F. J. Walburn, D. J. Schneck, A constitutive equation for whole human blood, *Biorheology* 13 (3) (1976) 201–210. doi:10.3233/BIR-1976-13307.
- [20] R. Mehri, C. Mavriplis, M. Fenech, Red blood cell aggregates and their effect on non-Newtonian blood viscosity at low hematocrit in a two-fluid low shear rate microfluidic system, *PLOS ONE* 13 (7) (2018) e0199911. doi:10.1371/journal.pone.0199911.
- [21] M. Mendlowitz, The Effect of Anemia and Polycythemia on Digital Intravascular Blood Viscosity, *The Journal of Clinical Investigation* 27 (5) (1948) 565–571. doi:10.1172/JCI102001.
- [22] S. Kundrapu, J. Noguez, Chapter Six - Laboratory Assessment of Anemia, in: G. S. Makowski (Ed.), *Advances in Clinical Chemistry*, Vol. 83, Elsevier, 2018, pp. 197–225. doi:10.1016/bs.acc.2017.10.006.
- [23] H. H. Billett, Hemoglobin and Hematocrit, in: H. K. Walker, W. D. Hall, J. W. Hurst (Eds.), *Clinical Methods: The History, Physical, and Laboratory Examinations*, 3rd Edition, Butterworths, Boston, 1990.
- [24] L. Václavů, Z. A. V. Baldew, S. Gevers, H. J. M. M. Mutsaerts, K. Fijnvandraat, M. H. Cnossen, C. B. Majoie, J. C. Wood, E. VanBavel, B. J. Biemond, P. van Ooij, A. J. Nederveen, Intracranial 4D flow magnetic resonance imaging reveals altered haemodynamics in sickle cell disease, *British Journal of Haematology* 180 (3) (2018) 432–442. doi:10.1111/bjh.15043.
- [25] A. Riva, F. Sturla, A. Caimi, S. Pica, D. Giese, P. Milani, G. Palladini, M. Lombardi, A. Redaelli, E. Votta, 4D flow evaluation of blood non-Newtonian behavior in left ventricle flow analysis, *Journal of Biomechanics* 119 (2021) 110308. doi:10.1016/j.jbiomech.2021.110308.
- [26] A. L. Cheng, C. P. Wee, N. M. Pahlevan, J. C. Wood, A 4D flow MRI evaluation of the impact of shear-dependent fluid viscosity on in vitro Fontan circulation flow, *American Journal of Physiology-Heart and Circulatory Physiology* 317 (6) (2019) H1243–H1253. doi:10.1152/ajpheart.00296.2019.
- [27] H. H. Yeh, O. Barannyk, D. Grecov, P. Oshkai, The influence of hematocrit on the hemodynamics of artificial heart valve using fluid-structure interaction analysis, *Computers in Biology and Medicine* 110 (2019) 79–92. doi:10.1016/j.combiomed.2019.05.003.
- [28] L. Formaggia, A. Quarteroni, A. Veneziani, *Cardiovascular Mathematics. Modeling and simulation of the circulatory system.*, Vol. 1, Springer, 2009.
- [29] A. Fasano, A. Sequeira, *Hemomath: The Mathematics of Blood*, Springer, 2017. doi:https://doi.org/10.1007/978-3-319-60513-5.
- [30] G. Arbia, I. Vignon-Clementel, T.-Y. Hsia, J.-F. Gerbeau, Modified navier–stokes equations for the outflow boundary conditions in hemodynamics, *European Journal of Mechanics - B/Fluids* 60 (2016) 175–188. doi:https://doi.org/10.1016/j.euromechflu.2016.06.001.
- [31] C. Bertoglio, R. Nuñez, F. Galarce, D. Nordsletten, A. Osses, Relative pressure estimation from velocity measurements in blood flows: State-of-the-art and new approaches, *International Journal for Numerical Methods in Biomedical Engineering* 34 (2) (2018) e2925. doi:https://doi.org/10.1002/cnm.2925.
- [32] F. Galarce, J. Gerbeau, D. Lombardi, O. Mula, Fast reconstruction of 3D blood flows from Doppler ultrasound images and reduced models, *Computer Methods in Applied Mechanics and Engineering* 375 (2021) 113559. doi:https://doi.org/10.1016/j.cma.2020.113559.
- [33] C. Fariás, C. Bayona-Roa, E. Castillo, R. C. Cabrales, R. Reyes, Reduced order modeling of parametrized pulsatile blood flows: Hematocrit percentage and heart rate, *International Journal of Engineering Science* 193 (2023) 103943. doi:https://doi.org/10.1016/j.ijengsci.2023.103943.
- [34] S. Katz, A. Caiazzo, V. John, Impact of viscosity modeling on the simulation of aortic blood flow, *Journal of Computational and Applied Mathematics* 425 (2023) 115036. doi:10.1016/j.cam.2022.115036.
- [35] S. Lynch, N. Nama, C. A. Figueroa, Effects of non-Newtonian viscosity on arterial and venous flow and transport, *Scientific Reports* 12 (1) (2022) 20568. doi:10.1038/s41598-022-19867-1.
- [36] D. Nolte, C. Bertoglio, Inverse problems in blood flow modeling: A review, *International Journal for Numerical Methods in Biomedical Engineering* (2022).
- [37] F. Galarce, D. Lombardi, O. Mula, Reconstructing haemodynamics quantities of interest from doppler ultrasound imaging, *International Journal for Numerical Methods in Biomedical Engineering* 37 (2) (2021) e3416. doi:https://doi.org/10.1002/cnm.3416.
- [38] H. Mella, J. Mura, J. Sotelo, S. Uribe, A comprehensive comparison between shortest-path HARP refinement, SinMod, and DENSE analysis processing tools applied to CSPAMM and DENSE images, *Magnetic Resonance Imaging* 83 (2021) 14–26. doi:10.1016/j.mri.2021.07.001.
- [39] H. Mella, J. Mura, H. Wang, M. D. Taylor, R. Chabiniok, J. Tintera, J. Sotelo, S. Uribe, HARP-I: A Harmonic Phase Interpolation Method

- for the Estimation of Motion from Tagged MR Images, *IEEE Transactions on Medical Imaging* 40 (4) (2021) 1240–1252. doi:10.1109/TMI.2021.3051092.
- [40] PyMRStrain, a Python library for the generation of synthetic MR strain phantoms, <https://github.com/hmella/pymrstrain/tree/4dflow>.
- [41] N. M. Wilson, A. K. Ortiz, A. B. Johnson, The vascular model repository: A public resource of medical imaging data and blood flow simulation results, *Journal of Medical Devices* 7 (40923) (2013-12-05). doi:10.1115/1.4025983.
- [42] M. R. Pfaller, J. Pham, A. Verma, L. Pegolotti, N. M. Wilson, D. W. Parker, W. Yang, A. L. Marsden, Automated generation of 0d and 1d reduced-order models of patient-specific blood flow, *International Journal for Numerical Methods in Biomedical Engineering* 38 (10) (2022) e3639. doi:10.1002/cnm.3639.
- [43] Vascular Model Repository, <https://www.vascularmodel.com/>.
- [44] V. Jhon, *Finite Element Methods for Incompressible Flow Problems*, Springer, 2016.
- [45] F. Brezzi, J. Pitkaranta, On the stabilization of finite element approximations of the stokes equations, *Efficient Solutions of Elliptic Systems* (1984).
- [46] A. N. Brooks, T. J. Hughes, Streamline upwind/ Petrov-galerkin formulations for convection dominated flows with particular emphasis on the incompressible navier-stokes equations, *Computer Methods in Applied Mechanics and Engineering* 32 (1) (1982) 199–259. doi:https://doi.org/10.1016/0045-7825(82)90071-8.
- [47] T. E. Tezduyar, Stabilized Finite Element Formulations for Incompressible Flow Computations, in: J. W. Hutchinson, T. Y. Wu (Eds.), *Advances in Applied Mechanics*, Vol. 28, Elsevier, 1991, pp. 1–44. doi:10.1016/S0065-2156(08)70153-4.
- [48] A. González, R. Cabrales, E. Castillo, Numerical study of the use of residual- and non-residual-based stabilized vms formulations for incompressible power-law fluids, *Computer Methods in Applied Mechanics and Engineering* 400 (2022) 115586. doi:https://doi.org/10.1016/j.cma.2022.115586.
- [49] R. Reyes, O. Ruz, C. Bayona-Roa, E. Castillo, A. Tello, Reduced order modeling for parametrized generalized newtonian fluid flows, *Journal of Computational Physics* 484 (2023) 112086. doi:https://doi.org/10.1016/j.jcp.2023.112086.
- [50] M. Esmaily Moghadam, Y. Bazilevs, T.-Y. Hsia, I. E. Vignon-Clementel, A. L. Marsden, Modeling of Congenital Hearts Alliance (MOCHA), A comparison of outlet boundary treatments for prevention of backflow divergence with relevance to blood flow simulations, *Computational Mechanics* 48 (3) (2011) 277–291. doi:10.1007/s00466-011-0599-0.
- [51] M. Esmaily Moghadam, I. E. Vignon-Clementel, R. Figliola, A. L. Marsden, A modular numerical method for implicit 0D/3D coupling in cardiovascular finite element simulations, *Journal of Computational Physics* 244 (2013) 63–79. doi:10.1016/j.jcp.2012.07.035.
- [52] F. Galarce Marin, Inverse problems in hemodynamics. fast estimation of blood flows from medical data. <https://gitlab.com/felipe.galarce.m/mad/>, Ph.D. thesis, INRIA Paris & Laboratoire Jacques-Louis Lions. Sorbonne Université (2021).
- [53] S. Balay, S. Abhyankar, A. M.D., J. Brown, P. Brune, K. Buschelman, L. Dalcin, V. Eijkhout, W. Gropp, D. Kaushik, M. Knepley, L. McInnes, K. Rupp, B. Smith, S. Zampini, H. Zhang, *PETSc Web page* (2015). URL <http://www.mcs.anl.gov/petsc>
- [54] M. M. Bissell, F. Raimondi, L. Ait Ali, B. D. Allen, A. J. Barker, A. Bolger, N. Burris, C.-J. Carhäll, J. D. Collins, T. Ebbers, C. J. Francois, A. Frydrychowicz, P. Garg, J. Geiger, H. Ha, A. Hennemuth, M. D. Hope, A. Hsiao, K. Johnson, S. Kozzerke, L. E. Ma, M. Markl, D. Martins, M. Messina, T. H. Oechtering, P. van Ooij, C. Rigsby, J. Rodriguez-Palomares, A. A. W. Roest, A. Roldán-Alzate, S. Schnell, J. Sotelo, M. Stuber, A. B. Syed, J. Töger, R. van der Geest, J. Westenberg, L. Zhong, Y. Zhong, O. Wieben, P. Dyverfeldt, 4D Flow cardiovascular magnetic resonance consensus statement: 2023 update, *Journal of Cardiovascular Magnetic Resonance* 25 (1) (2023) 40. doi:10.1186/s12968-023-00942-z.
- [55] J. A. Bender, R. Ahmad, O. P. Simonetti, The importance of k-space trajectory on off-resonance artifact in segmented echo-planar imaging, *Concepts in Magnetic Resonance Part A: Bridging Education and Research* 42 A (2) (2013) 23–31. doi:10.1002/cmr.a.21255.
- [56] H. Dillinger, J. Walheim, S. Kozzerke, On the limitations of echo planar 4D flow MRI, *Magnetic Resonance in Medicine* 84 (4) (2020) 1806–1816. doi:10.1002/mrm.28236.
- [57] A. T. Hess, M. M. Bissell, N. A. Ntusi, A. J. Lewis, E. M. Tunnicliffe, A. Greiser, A. F. Stalder, J. M. Francis, S. G. Myerson, S. Neubauer, M. D. Robson, Aortic 4D flow: Quantification of signal-to-noise ratio as a function of field strength and contrast enhancement for 1.5T, 3T, and 7T, *Magnetic Resonance in Medicine* 73 (5) (2015) 1864–1871. doi:10.1002/mrm.25317.
- [58] M. Barth, E. Moser, Proton NMR relaxation times of human blood samples at 1.5 T and implications for functional MRI, *Cellular and Molecular Biology (Noisy-Le-Grand, France)* 43 (5) (1997) 783–791.
- [59] S. Schnell, M. Markl, P. Entezari, R. J. Mahadewia, E. Semaan, Z. Stankovic, J. Collins, J. Carr, B. Jung, K-t GRAPPA accelerated four-dimensional flow MRI in the aorta: Effect on scan time, image quality, and quantification of flow and wall shear stress, *Magnetic Resonance in Medicine* 72 (2) (2014) 522–533. doi:10.1002/mrm.24925.
- [60] A. Pathrose, L. Ma, H. Berhane, M. B. Scott, K. Chow, C. Forman, N. Jin, A. Serhal, R. Avery, J. Carr, M. Markl, Highly accelerated aortic 4D flow MRI using compressed sensing: Performance at different acceleration factors in patients with aortic disease, *Magnetic Resonance in Medicine* 85 (4) (2021) 2174–2187. doi:10.1002/mrm.28561.
- [61] L. Desai, H. Stefek, H. Berhane, J. Robinson, C. Rigsby, M. Markl, Four-Dimensional flow Magnetic Resonance Imaging for Assessment of Pediatric Coarctation of the Aorta, *Journal of Magnetic Resonance Imaging* 55 (1) (2022) 200–208. doi:10.1002/jmri.27802.
- [62] J. Sotelo, L. Dux-Santoy, A. Guala, J. Rodríguez-Palomares, A. Evangelista, C. Sing-Long, J. Urbina, J. Mura, D. E. Hurtado, S. Uribe, 3D axial and circumferential wall shear stress from 4D flow MRI data using a finite element method and a laplacian approach, *Magnetic Resonance in Medicine* 79 (5) (2018) 2816–2823. doi:10.1002/mrm.26927.
- [63] M. Cherry, Z. Khatir, A. Khan, M. Bissell, The impact of 4D-Flow MRI spatial resolution on patient-specific CFD simulations of the thoracic aorta, *Scientific Reports* 12 (1) (2022) 15128. doi:10.1038/s41598-022-19347-6.
- [64] E. Ferdian, D. J. Dubowitz, C. A. Mauger, A. Wang, A. A. Young, WSSNet: Aortic Wall Shear Stress Estimation Using Deep Learning on 4D Flow MRI, *Frontiers in Cardiovascular Medicine* 8 (2022).
- [65] 4d-flow-matlab-toolbox, <https://github.com/JulioSoteloParraguez/4D-Flow-Matlab-Toolbox>.
- [66] J. Sotelo, J. Urbina, I. Valverde, C. Tejos, P. Irarrazaval, M. E. Andia, S. Uribe, D. E. Hurtado, 3d quantification of wall shear stress and oscillatory shear index using a finite-element method in 3d cine pc-mri data of the thoracic aorta, *IEEE Transactions on Medical Imaging*

- 35 (6) (2016) 1475–1487. doi:10.1109/TMI.2016.2517406.
- [67] K. Iwata, T. Sekine, J. Matsuda, M. Tachi, Y. Imori, Y. Amano, T. Ando, M. Obara, G. Crelier, M. Ogawa, H. Takano, S. Kumita, Measurement of Turbulent Kinetic Energy in Hypertrophic Cardiomyopathy Using Triple-velocity Encoding 4D Flow MR Imaging, *Magnetic Resonance in Medical Sciences* 23 (1) (2024) 39–48. doi:10.2463/mrms.mp.2022-0051.
- [68] S. Petersson, P. Dyverfeldt, T. Ebbers, Assessment of the accuracy of MRI wall shear stress estimation using numerical simulations, *Journal of Magnetic Resonance Imaging* 36 (1) (2012) 128–138. doi:10.1002/jmri.23610.
- [69] P. Dyverfeldt, M. Bissell, A. J. Barker, A. F. Bolger, C.-J. Carlhäll, T. Ebbers, C. J. Francios, A. Frydrychowicz, J. Geiger, D. Giese, M. D. Hope, P. J. Kilner, S. Kozerke, S. Myerson, S. Neubauer, O. Wieben, M. Markl, 4D flow cardiovascular magnetic resonance consensus statement, *Journal of Cardiovascular Magnetic Resonance* 17 (1) (2015) 72. doi:10.1186/s12968-015-0174-5.
- [70] M. Cibis, W. V. Potters, F. J. Gijzen, H. Marquering, P. van Ooij, E. vanBavel, J. J. Wentzel, A. J. Nederveen, The Effect of Spatial and Temporal Resolution of Cine Phase Contrast MRI on Wall Shear Stress and Oscillatory Shear Index Assessment, *PLOS ONE* 11 (9) (2016) e0163316. doi:10.1371/journal.pone.0163316.
- [71] J. F. Rodríguez-Palomares, L. Dux-Santoy, A. Guala, R. Kale, G. Maldonado, G. Teixidó-Turà, L. Galian, M. Huguet, F. Valente, L. Gutiérrez, T. González-Alujas, K. M. Johnson, O. Wieben, D. García-Dorado, A. Evangelista, Aortic flow patterns and wall shear stress maps by 4D-flow cardiovascular magnetic resonance in the assessment of aortic dilatation in bicuspid aortic valve disease, *Journal of Cardiovascular Magnetic Resonance* 20 (1) (2018) 28. doi:10.1186/s12968-018-0451-1.
- [72] J. Szajer, K. Ho-Shon, A comparison of 4D flow MRI-derived wall shear stress with computational fluid dynamics methods for intracranial aneurysms and carotid bifurcations — A review, *Magnetic Resonance Imaging* 48 (2018) 62–69. doi:10.1016/j.mri.2017.12.005.
- [73] J. V. Soulis, G. D. Giannoglou, Y. S. Chatzizisis, K. V. Seralidou, G. E. Parcharidis, G. E. Louridas, Non-Newtonian models for molecular viscosity and wall shear stress in a 3D reconstructed human left coronary artery, *Medical Engineering & Physics* 30 (1) (2008) 9–19. doi:10.1016/j.medengphy.2007.02.001.
- [74] S. Karimi, M. Dabagh, P. Vasava, M. Dadvar, B. Babir, P. Jalali, Effect of rheological models on the hemodynamics within human aorta: CFD study on CT image-based geometry, *Journal of Non-Newtonian Fluid Mechanics* 207 (2014) 42–52. doi:10.1016/j.jnnfm.2014.03.007.
- [75] P. A. Heidenreich, B. Bozkurt, D. Aguilar, L. A. Allen, J. J. Byun, M. M. Colvin, A. Deswal, M. H. Drazner, S. M. Dunlay, L. R. Evers, J. C. Fang, S. E. Fedson, G. C. Fonarow, S. S. Hayek, A. F. Hernandez, P. Khazanie, M. M. Kittleson, C. S. Lee, M. S. Link, C. A. Milano, L. C. Nwacheta, A. T. Sandhu, L. W. Stevenson, O. Vardeny, A. R. Vest, C. W. Yancy, 2022 AHA/ACC/HFSA Guideline for the Management of Heart Failure: A Report of the American College of Cardiology/American Heart Association Joint Committee on Clinical Practice Guidelines, *Circulation* 145 (18) (2022) e895–e1032. doi:10.1161/CIR.0000000000001063.
- [76] G. Jacob, S. R. Raj, T. Ketch, B. Pavlin, I. Biaggioni, A. C. Ertl, D. Robertson, Postural Pseudoanemia: Posture-Dependent Change in Hematocrit, *Mayo Clinic Proceedings* 80 (5) (2005) 611–614. doi:10.4065/80.5.611.
- [77] H. P. Sennels, H. L. Jørgensen, A.-L. S. Hansen, J. P. Goetze, J. Fahrenkrug, Diurnal variation of hematology parameters in healthy young males: The Bispebjerg study of diurnal variations, *Scandinavian Journal of Clinical and Laboratory Investigation* 71 (7) (2011) 532–541. doi:10.3109/00365513.2011.602422.
- [78] J. M. Hilderink, L. J. J. Klinkenberg, K. M. Aakre, N. C. J. de Wit, Y. M. C. Henskens, N. van der Linden, O. Bekers, R. J. M. W. Rennenberg, R. P. Koopmans, S. J. R. Meex, Within-day biological variation and hour-to-hour reference change values for hematological parameters, *Clinical Chemistry and Laboratory Medicine (CCLM)* 55 (7) (2017) 1013–1024. doi:10.1515/cc1m-2016-0716.
- [79] B. E. Statland, P. Winkel, S. C. Harris, M. J. Burdsall, A. M. Saunders, Evaluation of Biologic Sources of Variation of Leukocyte Counts and Other Hematologic Quantities Using Very Precise Automated Analyzers, *American Journal of Clinical Pathology* 69 (1) (1978) 48–54. doi:10.1093/ajcp/69.1.48.
- [80] M. Maes, S. Scharpé, W. Cooreman, A. Wauters, H. Neels, R. Verkerd, F. De Meyer, P. D'Hondt, D. Peeters, P. Cosyns, Components of biological, including seasonal, variation in hematological measurements and plasma fibrinogen concentrations in normal humans, *Experientia* 51 (2) (1995) 141–149. doi:10.1007/BF01929358.
- [81] P. Thirup, Haematocrit, *Sports Medicine* 33 (3) (2003) 231–243. doi:10.2165/00007256-200333030-00005.
- [82] M.-Y. Su, Y.-S. Huang, E. Niisato, K. Chow, J.-M. J. Juang, C.-K. Wu, H.-Y. Yu, L.-Y. Lin, S.-C. Yang, Y.-C. Chang, Is a timely assessment of the hematocrit necessary for cardiovascular magnetic resonance-derived extracellular volume measurements?, *Journal of Cardiovascular Magnetic Resonance* 22 (1) (2020) 77. doi:10.1186/s12968-020-00689-x.